© 2016. Published by The Company of Biologists Ltd | Journal of Experimental Biology (2016) 219, 752-766 doi:10.1242/jeb.127829

RESEARCH ARTICLE

Surface tension dominates insect flight on fluid interfaces

Haripriya Mukundarajan[1], Thibaut C. Bardon[2], Dong Hyun Kim[1] and Manu Prakash[3,*]

ABSTRACT

Flight on the 2D air–water interface, with body weight supported by surface tension, is a unique locomotion strategy well adapted for the environmental niche on the surface of water. Although previously described in aquatic insects like stoneflies, the biomechanics of interfacial flight has never been analysed. Here, we report interfacial flight as an adapted behaviour in waterlily beetles (*Galerucella nymphaeae*) which are also dexterous airborne fliers. We present the first quantitative biomechanical model of interfacial flight in insects, uncovering an intricate interplay of capillary, aerodynamic and neuromuscular forces. We show that waterlily beetles use their tarsal claws to attach themselves to the interface, via a fluid contact line pinned at the claw. We investigate the kinematics of interfacial flight trajectories using high-speed imaging and construct a mathematical model describing the flight dynamics. Our results show that non-linear surface tension forces make interfacial flight energetically expensive compared with airborne flight at the relatively high speeds characteristic of waterlily beetles, and cause chaotic dynamics to arise naturally in these regimes. We identify the crucial roles of capillary–gravity wave drag and oscillatory surface tension forces which dominate interfacial flight, showing that the air–water interface presents a radically modified force landscape for flapping wing flight compared with air.

KEY WORDS: Interfacial flight, Biomechanics, Capillary waves, Capillary–gravity wave drag, Chaos

INTRODUCTION

Insects constitute the majority of living species on land (May, 1988). Flight has played a crucial role in the proliferation of insects, enabling them to explore and adapt to new habitats, evade predators and find mates (Simon et al., 2009). About 98% of insect species are capable of powered airborne flight (Simon et al., 2009), the intricate biomechanics and origins of which have captivated physicists, engineers and biologists for centuries. One phenomenon proposed as a hypothesis for the origin of flight is surface skimming, where wings or wing-like structures are used to generate propulsion along an air–water interface (Marden et al., 2000; Marden, 2003). Flight along a fluid interface is a fascinating mode of insect locomotion that is far less studied than other modes of locomotion. Several aquatic species of stoneflies and mayflies use their wings to row, sail or flap along the air–water interface. Some of these have rudimentary wings and cannot generate sufficient lift to completely support their body weight in air, whereas others use surface skimming in a context-dependent fashion, mostly under conditions such as cold temperatures that do not permit airborne flight. A competing evolutionary hypothesis poses directed gliding as the origin of insect flight (Dudley and Yanoviak, 2011; Dudley et al., 2007), based on observations and biomechanical analysis of creatures such as the canopy ant *Cephalotus atratus* (Yanoviak et al., 2005). The relative merits of different flight origin hypotheses have so far been discussed by comparing observational, molecular and fossil evidence, and lie outside the scope of our current study. However, a quantitative understanding of interfacial flight phenomena is a crucial requirement for a better appreciation and comparative evaluation of these ideas. In this work, we present the first biomechanical model describing the physics underlying flight along a fluid interface, to elucidate the roles of capillary, aerodynamic and neuromuscular forces in giving rise to this rare and complex locomotive behaviour.

Here, we define interfacial flight as biomechanically powered flapping-wing locomotion where the insect's trajectory is limited to the 2D plane of an air–water interface. The spatial degrees of freedom of the insect's trajectory are now reduced from six to just three. Although the insect's body weight is supported by surface tension, other complications arise due to contact with water. First, water is 50 times more viscous than air. Further, capillary forces can be as high as a few hundred times the viscous drag during interfacial flight. Additionally, the insect generates capillary waves or ripples when moving along the interface, which produce non-linear drag effects depending upon the speed of motion. Finally, the forces exerted by surface tension that keep an insect attached to the interface are dependent on the wetting properties of its body parts in contact with water. This resultant force of surface tension can be comparable to or greater than the body weight. It can either be directed upwards (supporting an insect's body weight), as commonly seen in water-walking insects, or directed downwards (trapping an insect on the water surface), as commonly seen in insects that are unable to take off from a water surface when they become wetted. Overall, the non-linear effects of capillary forces and the complexity of contact line dynamics on insect body parts are not well understood. The phenomenon of interfacial flight and the transition to airborne flight thus presents intriguing puzzles for studies in physical biology.

Here, we report the observation of 2D interfacial flight over a wide range of speeds (Movie 1) as a derived adaptation of 3D airborne flight in waterlily beetles (*Galerucella nymphaeae*, Linnaeus 1758), which can also make smooth transitions between interfacial and airborne flight (Movie 2). This makes the waterlily beetle an ideal model organism to analyse the fundamental physics of interfacial flight and the stepwise transitions to airborne flight. Using high-speed videography, we recorded the kinematics of flight trajectories on the interface and identified features that are strongly influenced by capillary forces. We used our observations to develop a mathematical framework for modelling flapping wing propulsion naturally confined to a 2D fluid interface. Our results show that as locomotion velocities increase horizontally along the interface, interfacial flight becomes more energetically expensive because of the influence of capillary wave drag. In addition, a chaotic regime comes into existence as vertical lift forces increase at a given wing

[1]Department of Mechanical Engineering, Stanford University, Stanford, CA 94305, USA. [2]École Polytechnique, Paris, Palaiseau 91128, France. [3]Department of Bioengineering, Stanford University, Stanford, CA 94305, USA.

*Author for correspondence (manup@stanford.edu)

Received 3 July 2015; Accepted 21 December 2015

Journal of Experimental Biology

Journal of Experimental Biology (2016) 219, 752-766 doi:10.1242/jeb.127829

List of symbols and abbreviations

A_x	horizontal air drag on body
A_w	wing area
Bo	Bond number (defined as the ratio of weight to surface tension)
Ca	Capillary number (defined as the ratio of viscous to capillary forces)
$C_{D,body}$	body drag coefficient
$C_{D,leg}$	leg drag coefficient
C_L	lift coefficient
c_{min}	minimum phase velocity of capillary waves in water
C_x	horizontal capillary–gravity wave drag on legs
f_w	wingbeat frequency
g	acceleration due to gravity
G_y	vertical gravity body force
L_y	vertical wing lift
m	mass of the insect
p	thrust-to-lift ratio
r	ratio of upstroke force to downstroke force
R_{claw}	leg radius at the claw joint
Re	Reynolds number (defined as the ratio of inertial to viscous forces)
St	Strouhal number (defined as the ratio of added mass of water at the legs in each wingbeat to inertial forces)
S_y	surface tension
T_x	horizontal wing thrust
V_w	wingtip velocity
W_x, W_y	water drag on submerged claws (horizontal, vertical)
We	Weber number (defined as the ratio of inertial to capillary forces)
x	horizontal displacement along the interface
$\dot{x}$	horizontal velocity along the interface
y	vertical displacement normal to the interface
$\dot{y}$	vertical velocity normal to the interface
θ	contact angle of water meniscus at the claw joint
κ^{-1}	capillary length
ν	kinematic viscosity of water
ρ	density of water
σ	surface tension of water
ϕ_0	wing stroke angle at initiation of motion
ω	wing angular velocity

flapping frequency. These insights highlight that 2D interfacial flight is a complex non-linear phenomenon, whose unique kinematics differs significantly from that of purely airborne flight.

MATERIALS AND METHODS

About 400 live adult beetles (*G. nymphaeae* and *G. pusilla*) were captured in Harvard Forest (MA, USA) and in Montana during May–July over several years. These were maintained in the lab in an incubator at 18°C and 60% relative humidity with a 14 h:10 h light: dark cycle, and fed waterlily or loosestrife leaves collected at the capture site. Beetles were carefully transferred for experiments on water using a piece of waterlily leaf, to avoid touching them or accidentally wetting their legs prior to observation. One beetle at a time was placed in a Petri dish or small cage (200×150×100 mm) with ∼1 cm of standing water, and bits of leaves or green plastic pieces placed on the opposite end to initiate motion. All experiments were carried out in laboratory conditions where ambient temperature was maintained around 23°C, so as not to vary the surface tension of water.

For kinematic measurements, we took high-speed videos of interfacial flight at 3000 frames s^{-1} using a Phantom v1210 camera. Wide-field videos with a typical field of view around 250 mm but low resolution of the order of 100 µm per pixel were used to observe full flight trajectories (Movies 2–4). High-magnification videos with smaller fields of view around 100 mm but high resolution of the order of 10 µm per pixel were recorded to measure displacements and velocities for parts of some trajectories (Movies 1, 5 and 6). Certain points on the beetle's body, such as the eye, the mouthparts and the femur–tibia joint, stand out as high-contrast areas that can be used as natural markers. We used an in-house shape-tracking script to automate the extraction of coordinates of the centroids of these markers in each frame. Although a significant number of video runs were collected, only trajectories having sufficient pixel resolution that were also perfectly parallel to the imaging plane were chosen for quantitative analysis.

RESULTS

Discovery of interfacial flight in wild *G. nymphaeae*

We report the discovery of interfacial flight in beetles of the genus *Galerucella* (Fig. 1A,B; Movie 1). Unlike many other interfacial fliers, all species of *Galerucella* possess well-developed airborne flight capabilities [Movie 2 (parts B and C)]. However, some species like the waterlily beetle *G. nymphaeae* display a preference for interfacial flight, while others like the purple loosestrife beetle *G. calmariensis* are incapable of it. In the wild, waterlily beetles (*G. nymphaeae*, formerly *Pyrrhalta nymphaeae*) live on the surface of ponds where they feed on floating waterlily leaves. They react to visual cues of floating green objects, executing straight-line movements along the surface towards these objects at high speeds of over 50 body lengths per second (0.3 m s^{-1}). The preference for interfacial flight is pronounced under a variety of conditions, where we observed the beetles skimming along the interface between leaves at a variety of different temperatures between 14 and 28°C (ambient environmental conditions to laboratory conditions). We conjecture that, topologically, interfacial flight provides an efficient foraging strategy to feed on floating waterlily leaves on the planar water surface using motility that is also confined to a 2D plane.

Laboratory observations of interfacial flight

After preliminary observations in the field, we brought the waterlily beetles into the lab to record observations of interfacial flight. *Galerucella nymphaeae* prepares for flight along the interface by first lifting each leg off the surface and setting it back down. This avoids excessive wetting of the tarsi (where water displaces air from the gaps between the hydrophobic hairs on the leg) due to impact or other accidental contact, though fouling due to naturally occurring floating lipids in wild settings is not so readily overcome. Just before the start of interfacial flight, the beetle lifts its middle pair of legs off the water and angles its body upwards [Movie 1 (part A)]. This posture with only four legs in contact with water lowers the drag from the legs, but still provides a wide base to prevent falling over during flight. Such a posture also serves to place the legs out of the way of the stroke of the dominant hindwing. This is a significant difference compared with stoneflies and mayflies, which have dominant forewings and hence raise their forelegs up during skimming (Marden et al., 2000). The beetle flaps its wings to unfurl them fully, and sets up consistent, strong wingbeats, resulting in horizontal speeds of up to 0.5 m s^{-1}. This is not only fast relative to its body length of 6 mm but also in absolute terms, to the best of our knowledge, is among the fastest reported average horizontal speed for an insect on a fluid interface (Bush and Hu, 2006; Marden et al., 2000). The flapping of well-developed wings allows both force generation and high speeds to be continuously sustained over relatively long distances of a few metres (Fig. 1E,F). Though the insect itself is difficult to see during its quick movement, a striking visible manifestation of its motion is the continuous formation of a

Journal of Experimental Biology (2016) 219, 752-766 doi:10.1242/jeb.127829

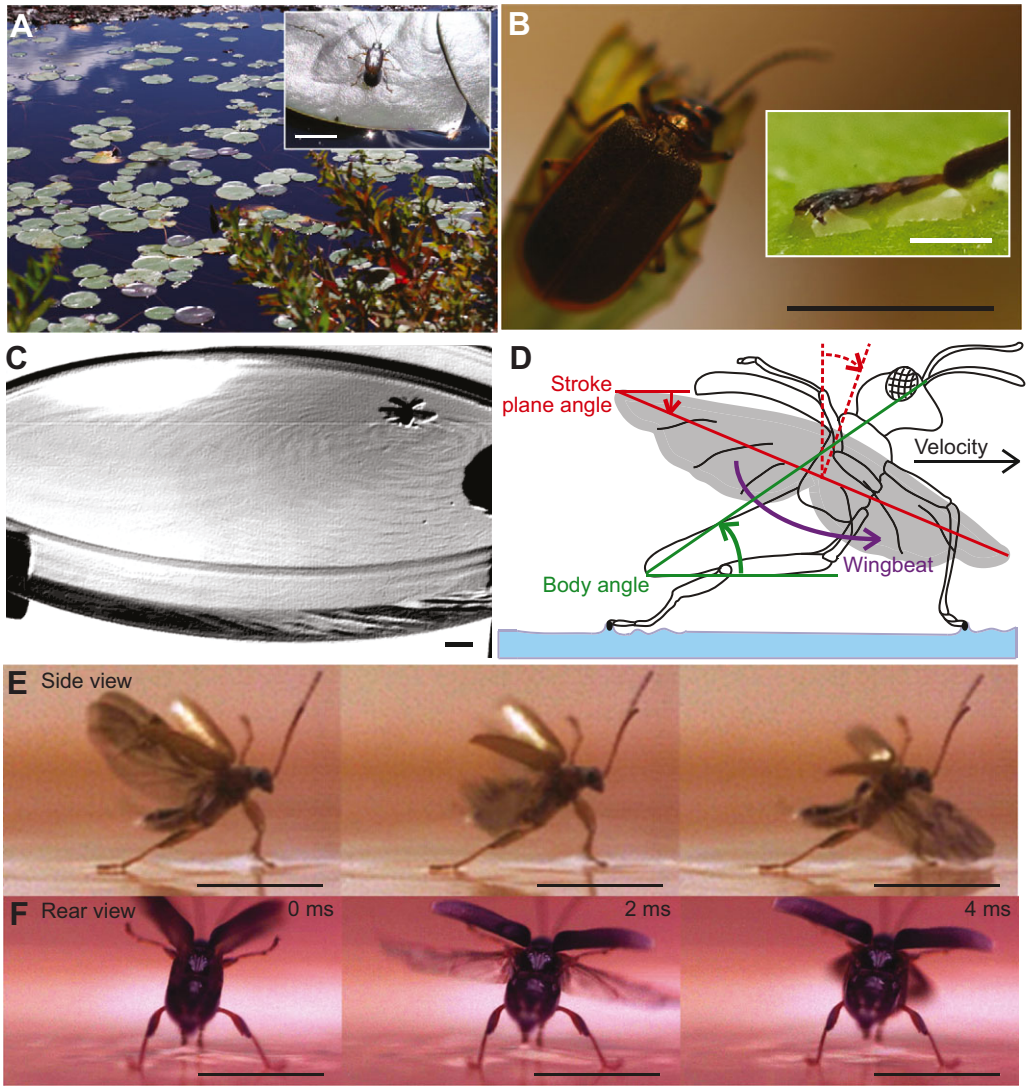

Fig. 1. Interfacial flight in *Galerucella nymphaeae*. (A) Natural habitat of *G. nymphaeae* in Harvard Forest, MA, USA, where the first specimens were observed and captured. Inset shows a wild specimen resting on a waterlily leaf. (B) Close-up of *G. nymphaeae*. Inset shows the leg resting on a drop of water, such that the tarsi are unwetted and supported on the drop while the claws at the tip are immersed in the water. Note that the drop is deformed near the claws. (C) Capillary waves are generated during interfacial flight, due to the perturbation of the interface by the insect's immersed claws. (D) Schematic illustration of interfacial flight in *G. nymphaeae*. (E,F) side view and rear view of *G. nymphaeae* posture in upstroke, midstroke and downstroke of interfacial flight. The middle pair of legs is raised above the body and the body is angled such that its weight is well supported between the four immersed legs. Scale bars 5 mm (1 mm in B inset).

train of capillary waves (ripples) around it (Fig. 1C; Movie 4). Such waves have also been reported in other surface-skimming stoneflies (Marden et al., 2000). They have also been shown to play an important role in the movement and behaviour of insects like whirligig beetles, which are partially submerged in water (Voise and Casas, 2010). This insight highlights the importance of considering capillary dissipation effects in interfacial flight analyses.

Structural adaptations enabling 2D flight in *G. nymphaeae*

Using electron microscopy, we discovered that the waterlily beetle's body and legs are covered in small, water-repellent setae that can form a plastron air bubble (Fig. 2B,D,E), thus making the entire body superhydrophobic. This observation is intuitive, as the insect does not become wet during its fast spurts of movement despite living on the water surface. More surprisingly, we found that the water-repellent tarsi of the legs actually end in a smooth hydrophilic pair of curved tarsal claws, which are submerged in the water. The difference in wetting properties between the tarsi and claws forms a very distinctive hydrophobic–hydrophilic line junction on the insect's legs. We hypothesized that the hydrophilic claws are used to anchor the insect to the interface during flight (Fig. 2A,C,I–K). Many aquatic insects have entirely superhydrophobic leg surfaces that support them on water without any submerged parts (Prakash and Bush, 2011). However, the presence of a boundary between non-wetting tarsi and wetting claws on *G. nymphaeae* instead pins the water meniscus at this boundary, with the tarsi in air and claws in water [Figs 1B (inset), 2J,K; Movies 1 (part B) and 5]. Here, the term pinning indicates that the contact line does not move relative to the leg of the beetle, and always remains at the line boundary between the tarsi and claws. Such differential wetting stabilizes the meniscus at this line junction (Barthlott et al., 2010), preventing the contact line from slipping up and down the claws. This ensures the continuous action of capillary forces at the tarsus–claw joint, allowing capillary effects to dramatically influence interfacial flight. Surface tension now counteracts not only the downward pull due to weight during wing upstroke but also the upward pull of wing forces during the downstroke. We estimate the maximum restoring force on four immersed legs to be equal to $4\times2\pi\sigma R_{\mathrm{claw}}\approx5\times mg\approx100$ μN, where σ=0.072 N m s^{-1} is the surface tension of water, R_{claw}=57 μm is the leg radius at the immersion point measured from the scanning electron micrograph in Fig. 2A, and m=2.2 mg is the mass of the insect found by averaging values measured for 30 recently deceased insects. The insect's body weight is supported by an opposite deflection of the meniscus which prevents sinking. This can be estimated by the non-dimensional Bond number (defined as the ratio of weight to surface tension, Bond

Journal of Experimental Biology (2016) 219, 752-766 doi:10.1242/jeb.127829

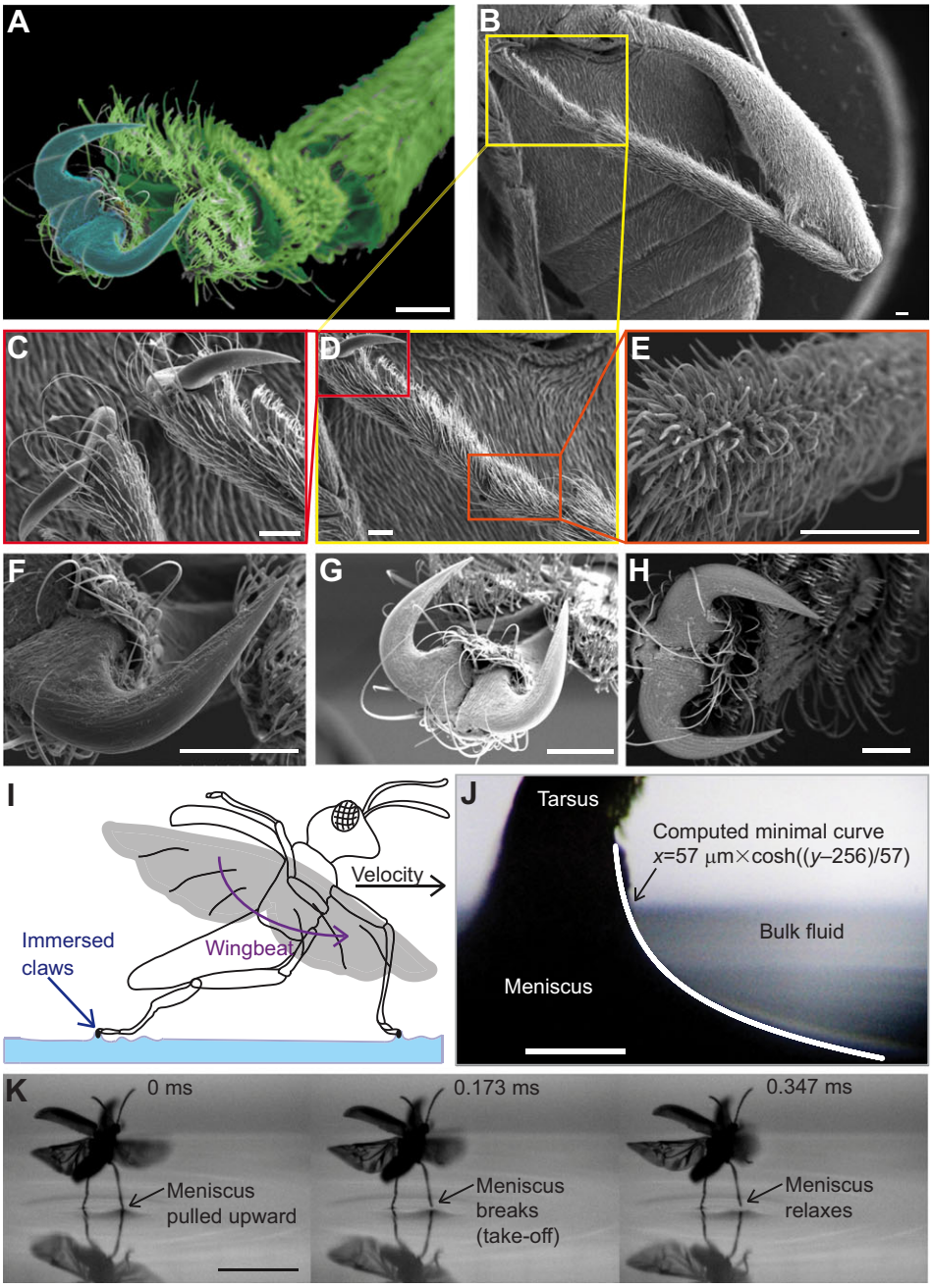

Fig. 2. Adaptations enabling interfacial flight in *G. nymphaeae*. (A) False colour SEM image indicating wetting and non-wetting regions on the leg. Green indicates superhydrophobic regions and blue indicates hydrophilic regions. (B) SEM images of *G. nymphaeae* body and legs showing hydrophobic hairy structures. (C–E) Successive magnifications of the hindleg ultrastructure (D) showing tarsi with hydrophobic setae (E), and a pair of curved, hydrophilic claws (C), which are immersed. (F–H) Similar hydrophobic–hydrophilic ultrastructural line barriers seen on hindlegs (F) and forelegs (G,H) of more beetles. (I) Schematic diagram showing pinning of the contact line at tarsal claws during interfacial flight. (J) Meniscus formed by dipping the leg of a dead beetle into water and raising up to the maximum extent. The white curve is the computed theoretical minimal surface profile, which fits the experimentally produced meniscus well. (K) Sequence showing formation and breakage of meniscus at the claw during take-off in a live beetle. White scale bars, 100 μm; black scale bar, 5 mm.

number $Bo_y \approx 0.2$). Thus, the force exerted by surface tension at the claw joint opposes both upward and downward motions of the beetle, constraining its flight to an effectively planar fluid interface.

Kinematics of interfacial flight trajectories

We first quantify the kinematics of flight on the 2D interface. The motion at the point of immersion of the beetle's legs is of maximum interest, as the effects of surface tension act directly to modify motion at this point. To extract immersion point trajectories, we tracked the femur–tibia joint, which is the closest natural high-contrast marker on the hindlegs. This joint is expected to follow the immersion point closely as there is no observed rotation of the intervening tarsal joints; hence, it was preferred over of the centre of mass of the beetle. One representative interfacial flight trajectory is shown in Fig. 3A, with a few additional trajectories in Fig. S1C,D for comparison. Trajectories recorded using markers other than the femur–tibia joint are shown in Fig. S1E,F, and have joint rotations and postural changes superimposed on the motion.

We identified five important kinematic trends which are characteristic of interfacial flight in *G. nymphaeae* and are all illustrated in the representative trajectory in Fig. 3A [extracted from Movie 1 (part A)]. First, the wingbeat frequency remains constant after the initial stages of flight initiation, with frequency measured at 116±5 Hz (Fig. S1A). Second, we observed a sigmoidal variation in horizontal displacement in each wingbeat, with the steepest increase occurring during the downstroke (Fig. 3B). Third, average horizontal velocity along the interface increases to values reaching 0.5 m s^{-1}, varying semi-sinusoidally in each wingbeat and reaching its maximum value during downstroke (Fig. 3C). The rate of increase of the average velocity is approximately piecewise, with varying accelerations

Journal of Experimental Biology (2016) 219, 752-766 doi:10.1242/jeb.127829

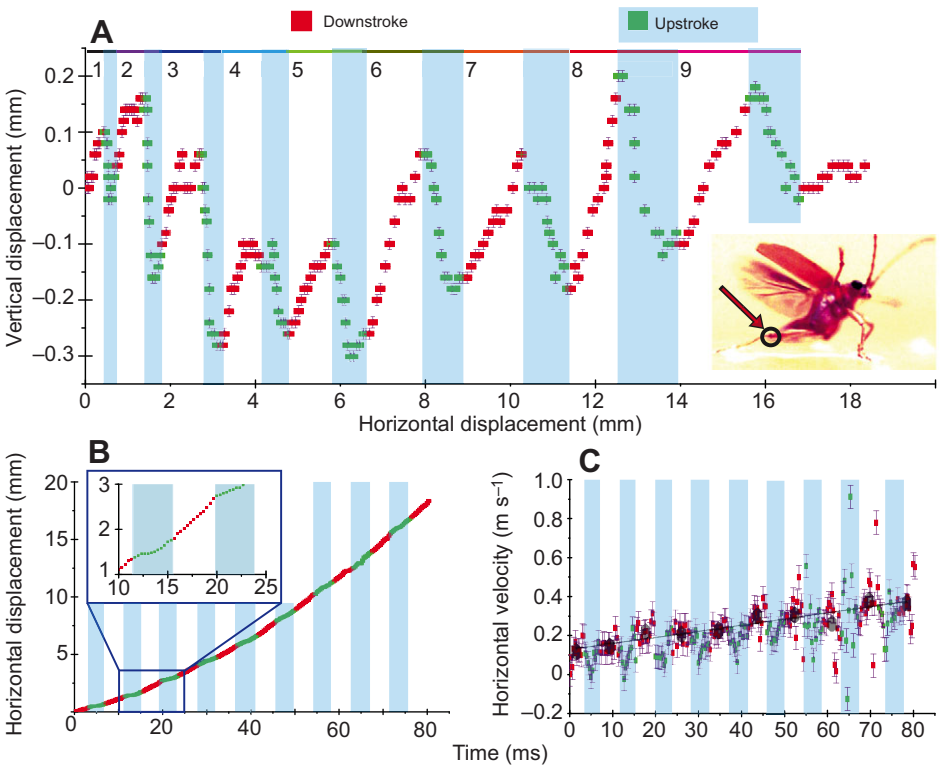

Fig. 3. Kinematics of interfacial flight trajectories. (A) Representative interfacial flight trajectory showing vertical oscillations. Inset shows a snapshot from the video used to generate the trajectory, with the arrow pointing to the femur–tibia joint of the insect's hindleg – a natural marker used for tracking. Error bars were calculated for tracked coordinates as the pixel resolution of the video, equal to approximately 10 µm per pixel. (B) Horizontal displacement increases rapidly, with average displacement per wingbeat varying quadratically with time. Inset shows the displacement during a single wingbeat, with a steep increase during downstroke and sigmoidal variation during upstroke. (C) Variation in horizontal velocity over time showing a linear increase in the average downstroke velocity. Velocity is maximum in the downstroke part of a wingbeat and drops to a minimum in mid-upstroke before recovering. Velocities were computed by fitting a spline to the displacement and calculating its slope. Error bars were derived from displacement errors.

above and below a cut-off velocity around 0.23 m s^{-1} (Fig. S1G). Fourth, at higher resolutions, we observed that the trajectory displays striking vertical oscillations perpendicular to the interfacial plane, which are often slightly phase shifted relative to the wingbeat. Such vibration with a shift in relative phase is the most intriguing feature of interfacial flight, and results from the interaction of a restoring surface tension force with oscillatory forces produced by the wings. The oscillations have a frequency close to the wingbeat and amplitude spanning between 300 and 500 µm, or up to 25% of the insect's dorso-ventral height of 2 mm. The maximum peak-to-peak displacement amplitudes are approximately equal to twice the theoretical maximum meniscus height that can be supported by gravity. (Assuming quasi-static zero-pressure deformation of the meniscus, twice the maximum height $2\times H_{max}=2\times R_{claw}\ \ln(2\kappa^{-1}/R_{claw})\approx 500$ µm, where $R_{claw}=57$ µm is the radius at the claw and $\kappa^{-1}=2.71$ mm is the capillary length.) This length scale is a fundamental characteristic of interfacial flight trajectories, and any further increase in oscillation amplitude would result in meniscus breakage and airborne flight. Thus, the amplitude of vertical oscillations in the trajectory determines the transition between interfacial and airborne flight. Accelerations due to the vertical oscillations are of the order of g, with variations of similar magnitude due to the relative phase between the wingbeat and the oscillations (data not shown). This shows that the oscillations contribute significantly to the dynamics of the trajectory with storage and release of energy from the water meniscus similar to a fluid trampoline (Gilet and Bush, 2009). Lastly, the peak displacement of each oscillation varies widely with each successive wingbeat, appearing as though there is an additional irregular variation superimposed on the oscillations at wingbeat frequency. We thus infer that the interactions between surface tension and wingbeat modify the oscillations from simple sinusoids to more complex trajectories, as the relationship between surface tension and vertical displacement is not a simple linear proportional dependence but a non-linear hyperbolic function. Taken together, these five trends highlight that non-linear oscillatory effects caused by surface tension modify interfacial flight trajectories significantly compared with airborne flight.

Force landscape during interfacial flight

The kinematic data in Fig. 3A allow us to estimate the relative importance of the forces involved in interfacial flight using non-dimensional parameters. To compare the importance of inertial and capillary forces, we calculate the Weber number, defined as the ratio of inertial to capillary forces: $We=\rho\dot{x}R_{claw}/\sigma$, where ρ is the density of water, $\dot{x}$ is the translational fluid velocity and R_{claw} is the characteristic length scale – the leg radius at the claw joint. For both horizontal and vertical motion, we obtained a fairly low Weber number of the order of 0.1 [$We\approx O(0.1)$], implying that capillary forces dominate. Next, we looked at the Reynolds number, defined as the ratio of inertial to viscous forces: $Re=\dot{x}R_{claw}/\nu$, where ν is the kinematic viscosity of the fluid. In both water and air, we find moderate values of $Re\approx O(10–100)$. We also compute the Strouhal number in water, defined as the ratio of added mass of water at the legs in each wingbeat to inertial forces, which yields a small value $St=fR_{claw}/\dot{x}\approx 0.02$, indicating that the added mass of water can safely be ignored. From this, we conclude that interfacial flight is dominated by capillary forces with smaller contributions from water inertia and aerodynamic forces, while viscous dissipation is small. To corroborate the relative dominance of capillary forces over viscous forces for horizontal motion, we show relatively low values of the Capillary number, defined as the ratio of viscous to capillary forces, around $Ca=\rho\nu\dot{x}/\sigma\approx 0.005$. The prominent role of capillary forces makes the physics of interfacial flight unique in comparison to both water-walking arthropods, where capillary forces are secondary to viscous drag (Bush and Hu, 2006; Suter et al., 1997), and also airborne flight,

Journal of Experimental Biology (2016) 219, 752-766 doi:10.1242/jeb.127829

where capillary effects are absent and aerodynamic forces prevail (Sane, 2003; Dickinson et al., 1999; Lehmann, 2008; Ellington, 1995). We now use these insights to construct a reduced-order model for interfacial flight, which captures the essential physical phenomena involved.

Dynamic model for interfacial flight

Here, we construct the simplest possible model of interfacial flight taking into account interfacial, viscous, gravitational and aerodynamic forces (Fig. 4). The dynamical analysis of interfacial flight can be greatly simplified by reducing the insect to a single particle pinned at the air–water interface with all forces acting directly on it, making the problem analytically tractable. We outline the main conceptual elements of our model here, with a detailed treatment of the mathematical equations and their validation provided in the Appendix. The interfacial contact is represented by the two forces of capillary–gravity wave drag C_x in the horizontal direction x along the interface (Raphael and de Gennes, 1996) and the resultant of surface tension S_y in the vertical direction y normal to the interface. Capillary–gravity wave drag C_x is the dissipative force that arises when the insect moves at speeds sufficiently high to exceed the minimum phase velocity of capillary–gravity waves on the interface, causing its momentum to be radiated away by the waves. Forces arising from surface tension S_y must be modelled taking the specific nature of the contact into account, for the particular insect or interfacial system under consideration. There is considerable variation in the geometry of contact for the legs of different insects, such as line contact, contact through groups of penetrating hairs (Prakash and Bush, 2011) and also through penetrating hydrophilic ungui (Bush et al., 2008). Here, in the representative case of *G. nymphaeae*, we use a model corresponding to pinning of the meniscus at the line boundary between the superhydrophobic leg and the hydrophilic claw. Surface tension S_y is assumed to arise from the quasi-static deformation of non-interacting minimal surface menisci at each leg, which allows us to simplify the force model by ignoring contact angle hysteresis and interactions between the menisci. The minimal surface assumption is verified by dipping the insect's claw into water and fitting a minimal surface profile to the image of the meniscus (Fig. 2J). The meniscus produces a resultant force of surface tension that is opposite to the direction of vertical displacement with a non-linear dependence on the vertical displacement (de Gennes et al., 2004), like a non-linear spring. Thus, surface tension both supports the insect's body weight and provides a restraint against pulling off the surface depending on the nature of the meniscus curvature. The forces common to both interfacial and airborne flight are the wing forces (horizontal wing thrust T_x and vertical wing lift L_y), air drag A and gravity G_y. As the submerged claw of the legs dissipate some energy in water, we also add the small drags W_x and W_y from the water bulk. By resolving forces along horizontal and vertical directions, our model describes the dynamics of interfacial flight by the two decoupled scalar equations in x and y:

$$m\ddot{x} = T_x - W_x - A_x - C_x, \quad (1)$$

$$m\ddot{y} = L_y - W_y - G_y - S_y. \quad (2)$$

This model of an insect in interfacial flight is equivalent to a particle pinned to the plane of the fluid interface and translating in-plane, while also executing forced damped non-linear oscillations out-of-plane. By simulating a variety of different trajectories and comparing them with experimental data, our model allows us to gain additional quantitative insight into the dynamics of interfacial flight. This model is broadly applicable to all modes of interfacial flight, and its individual force terms can be modified to represent various cases such as high-speed flight, wetting of legs or varying wing force as appropriate for different insects. Here, we apply our model to interfacial flight in *G. nymphaeae* and present our insights into the energetics and dynamics of high-speed interfacial flight and take-off into air.

Body angle can be varied to produce different modes of interfacial, airborne or backward flight

A correlation between increasing body angle and the progression from interfacial to airborne flight was first proposed when comparing the different modes of interfacial flight in stoneflies (Marden and Kramer, 1994; Marden et al., 2000). As *G. nymphaeae* displays more than one of these flight modes as well as airborne flight, this makes it an ideal organism to study the effect of postural changes on transitions between modes. We observed that take-off into air always begins with a postural change, usually a transition from 4-leg to 2-leg interfacial flight [Movies 2 (parts A–C) and 5]. In addition, we also observed many instances of backward flight where the insect's horizontal velocity is directed opposite to its dorso-ventral axis [Movie 2 (part D)]. Based on these observations, we hypothesized that postural changes, particularly related to the stroke plane and body angles (defined in Fig. 1D), are key to adopting different flight modes. Here, we define four distinct flight modes – interfacial 4-leg, interfacial 2-leg, airborne forward and airborne backward. We analysed videos of 12 different flight sequences containing one or more of these modes in each, and measured stroke plane and body angles of the insect in each wingbeat. In all four flight modes, the angle between the dorso-ventral axis and the stroke plane, corresponding to wing joint rotation in the sagittal plane, is confined to a narrow range spanning only 30 deg (Fig. S1B). This implies that a given body angle for the insect allows only a restricted range of stroke plane angles. Indeed, Fig. 5A shows that as body angle of the insect increases, the stroke plane angle correspondingly decreases in a strongly linear correlation. Further, with increasing body angle, the flight mode

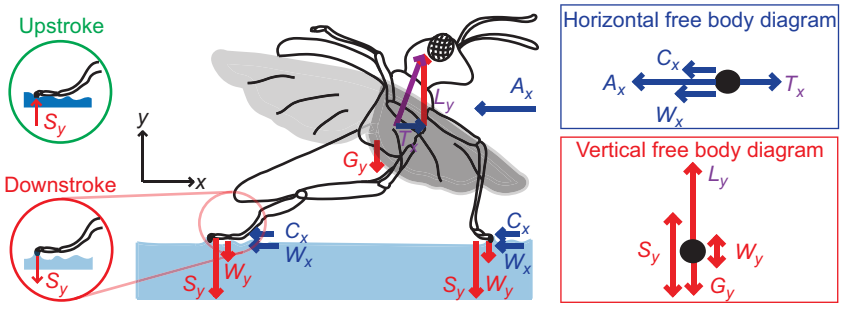

Fig. 4. Dynamic model for interfacial flight. Schematic diagram depicting the different forces acting on the beetle. Boxed insets on the right show the beetle reduced to a single particle pinned at the interface, with horizontal forces (top) and vertical forces (bottom) acting on the particle. Circled insets on the left show the direction reversal of surface tension, depending on the nature of deformation of the meniscus at the pinned contact line. A_x, horizontal air drag; C_x, horizontal capillary–gravity wave drag; T_x, horizontal thrust; W_x, horizontal water drag; G_y, vertical gravity (body weight); S_y, vertical resultant of surface tension; W_y, vertical water drag.

Journal of Experimental Biology (2016) 219, 752-766 doi:10.1242/jeb.127829

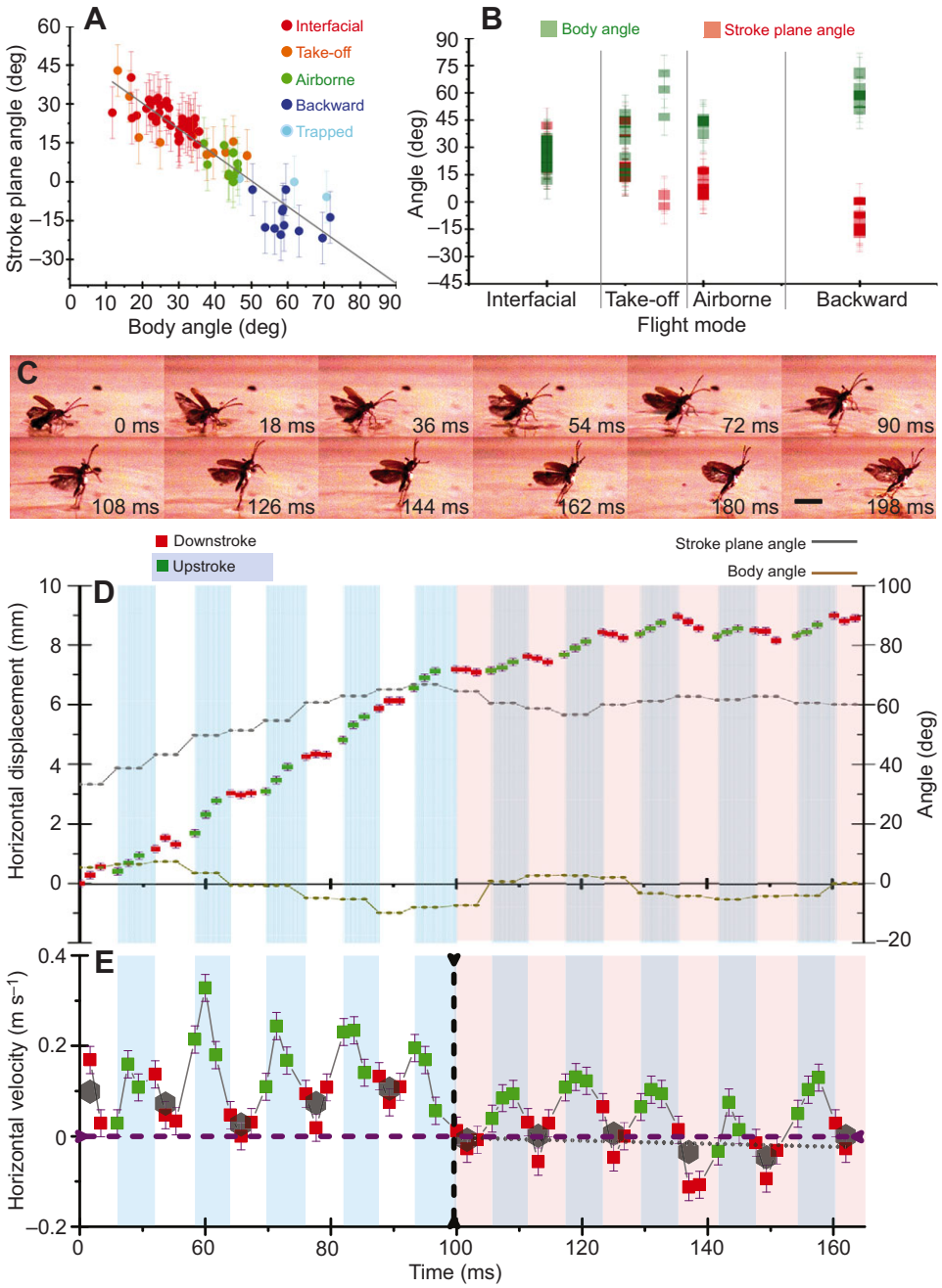

Fig. 5. Experimentally derived dynamics of wing forces exerted during interfacial flight. (A) Stroke plane angle decreases linearly as body angle increases during flight. Increasing body angle leads to transitions between interfacial, airborne or backward flight modes. Error bars are estimated from pixel resolution error in extreme wing and body points used to calculate angles. (B) As an insect takes off from the interface into air, body angle steadily increases while stroke plane angle approaches zero. When stroke plane angle falls below zero, the flight direction is backwards, opposite the dorsal-to-ventral axis. (C–E) Failed take-off attempt where the legs are trapped by surface tension. In C, a sequence of images shows a failed take-off attempt, where a significant portion of the legs is wetted. Note the almost vertical posture (body angle ~90 deg) that concentrates wing force into lift. Scale bar, 5 mm. (D) Horizontal displacement and body angle both increase initially, and then level off as thrust approaches zero (shaded region on the right.) Error bars indicate pixel resolution. (E) Mean horizontal velocity in each wingbeat is almost zero, resulting in a static equilibrium. Error bars were derived from positional errors corresponding to one pixel.

changes from interfacial to airborne to backward. This is evident in the distinct clustering of wingbeat data from different flight modes at different regions on the correlation line. Thus, the transition from interfacial to airborne to backward flight is characterized by increased body angle and decreased stroke plane angle (Fig. 5B). We propose that the insect transitions between flight modes by altering its stroke plane angle within the permissible joint rotation range, resulting in a torque on the body that changes the body angle. This change in body angle can be reduced, maintained or further increased through a feedback mechanism, where the stroke plane angle is respectively increased, kept constant or decreased again. We further hypothesize that this change in posture causes the variation in flight mode by altering the distribution between lift and thrust for the same net force exerted by the wings. Greater thrust at lower body angle corresponds to interfacial flight at high speeds, while greater lift at higher body angle corresponds to efficient vertical airborne flight. This is corroborated by using our model to run computer simulations of flight sequences at constant wing force and varying thrust-to-lift ratio p (Fig. 6B), where a series of trajectories smoothly varies from interfacial to airborne flight. Thus, we show that body angle is a critical parameter that can be tuned by an insect, altering the distribution of wing force between lift and thrust in order to achieve transitions between different modes of interfacial and airborne flight.

Wing lift can be estimated using surface tension

The majority of instances of interfacial flight in *G. nymphaeae* involve successful transitions to airborne flight [Fig. 2K; Movies 2 (parts A–C) and 5]. The successful take-off attempt in Movie 5 clearly shows the lifting of a meniscus to its maximum height and subsequent breaking at the instant of take-off. However, in some rare cases, take-off attempts naturally fail (Fig. 5C; Movie 6) as a

Journal of Experimental Biology (2016) 219, 752-766 doi:10.1242/jeb.127829

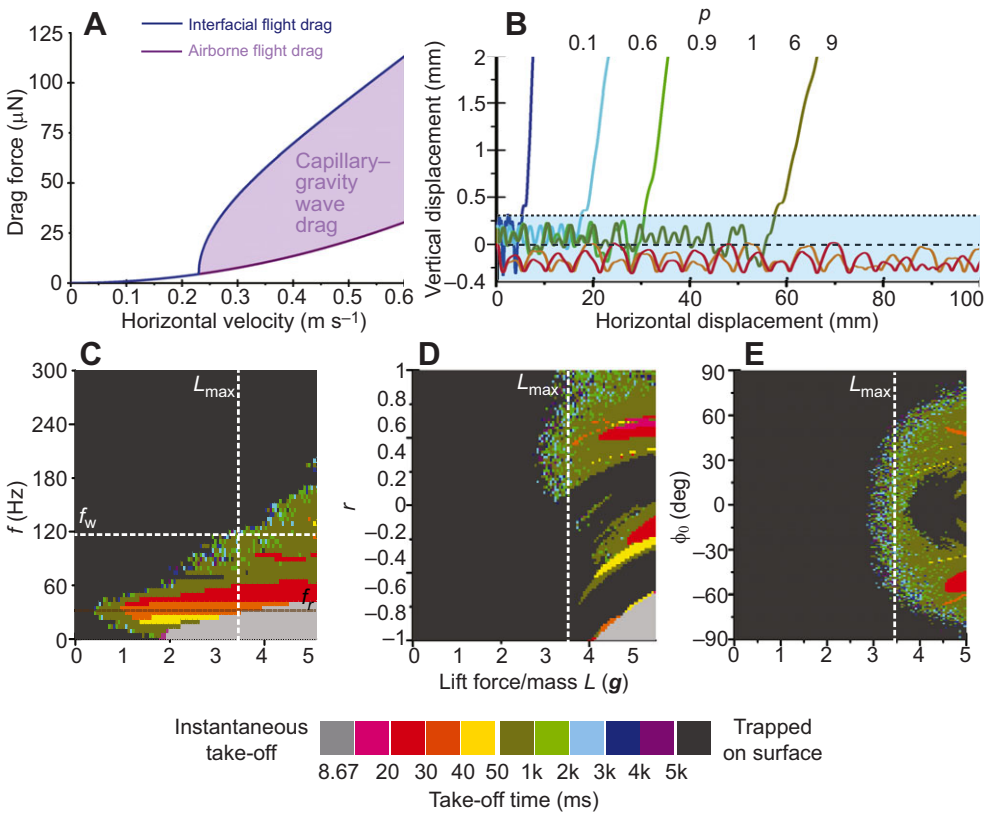

Fig. 6. Computational modelling of capillary drag, oscillations and take-off. (A) Comparison showing that total drag experienced in interfacial flight is much larger than that in airborne flight, above a critical velocity. The additional capillary–gravity wave drag experienced in interfacial flight is shown as the shaded region. (B) Different trajectories computed for a given total wing force magnitude, by varying the wing force distribution between lift and thrust. Trajectories take off for lower thrust-to-lift ratio p and remain confined to the interface for higher p. The dashed line is the mean water level at infinity and the dotted line is the maximum vertical height of meniscus attachment (260 μm). (C–E) Phase plots for variation in take-off time for different values of lift force per unit body weight, for an insect with two legs immersed in water. The single other parameter varied in each plot is wingbeat frequency f_w in C, symmetry ratio (r) between wing force produced in upstroke and downstroke in D, and wing stroke angle at initiation of motion (ϕ_0) in E. White dotted lines show the maximum estimated lift $L_{max}=2\times(2\pi R_{claw}\sigma)+mg$ and the wingbeat frequency $f_w\approx116$ Hz.

result of impacts, accidents or fouling, which cause water to be driven into the gaps between leg hairs and displace the air trapped within. This changes the wetting state of the legs, from the hydrophobic Cassie state, where an air layer reduces the water contact area, to the more hydrophilic Wenzel state, where the air is displaced and the contact line perimeter drastically increases (Bush et al., 2008). In the failed take-off in Movie 6, the insect transitions from 4-leg to 2-leg contact with the interface, angling its body almost vertically in an attempt to concentrate its entire wing force in the vertical direction for take-off (Fig. 5D). The insect comes to a halt in the horizontal direction as it now produces only lift and no thrust (Fig. 5E). The meniscus is lifted to its maximum height, and surface tension assumes its maximum value. However, in the current Wenzel state of wetting at the legs, surface tension no longer discontinuously drops to zero because of meniscus breakage, but maintains its maximum value as the leg now behaves like a wet fibre being pulled out of a fluid bath. In such a situation, the beetle is almost stationary and lift forces are balanced by surface tension and body weight. This corresponds to the 1D static equilibrium case in our model, where $\dot{x}$, $\ddot{x}$, $\dot{y}$, $\ddot{y}$, $T_x=0$. The model hence reduces to:

$$L_y = S_y + G_y. \quad (3)$$

This force equilibrium can be used to indirectly measure instantaneous wing forces using meniscus height. Forces measured under these special conditions help to establish upper bounds for typical lift forces exerted by an insect in normal interfacial flight, and provide a good estimate for the static force required to take off directly from the interface into air in the absence of oscillations. We estimated the maximum static lift force as $L_y=2\pi\sigma R_{claw}+mg\approx73$ μN, where $R_{claw}=57$ μm and $m=2.2$ mg. This corresponds to a lift coefficient of $C_L\approx1.55$, which is slightly higher than the typical C_L values of 1.1–1.4 measured experimentally for live tethered insects (Dudley, 2000; Dickinson et al., 1999) or found by computational methods (Sun and Tang, 2002). The lift-to-weight ratio is $q=3.4$, which is significantly higher than the typical values of 1–2.5 observed in airborne flight (Dudley, 2000), though it has been shown to be achievable in insects with high flight muscle ratios carrying maximal weights (Marden, 1987). (For detailed calculations of L_y, C_L and q, see the Appendix.) These increased C_L and q values indicate that the interfacial energy landscape can be thought of as an energy trap. For an insect without appropriate adaptations, making the transition from interfacial to airborne flight through purely quasi-static means would need much greater lift forces compared with typical airborne flight, primarily to escape the strong pull of surface tension.

Interfacial flight has higher total drag forces than airborne flight at typical speeds

The total drag force acting upon an insect in interfacial flight is the sum of the fluid resistance to motion arising from three sources: aerodynamic, hydrodynamic and capillary wave drags. Aerodynamic drags in interfacial and airborne flight are comparable, as the insect's body and wing area normal to air flow are about the same in both cases. However, an insect in interfacial flight has to contend with additional horizontal resistances from capillary–gravity wave drag and hydrodynamic drag, which we computed for *G. nymphaeae* using our model (Fig. 6A) (Chepelianskii et al., 2010). Capillary–gravity wave drag is absent at speeds below the threshold of $c_{min}=0.23$ m s^{-1}, but quickly exceeds air drag above this critical speed. At the typical speeds of 0.3–0.5 m s^{-1} observed in interfacial flight in *G. nymphaeae*, capillary–gravity wave drag is several times higher than aerodynamic drag, meaning that it is much easier for an insect to fly in air than skim along the interface. Total drag forces in interfacial and airborne flight do converge to comparable values at

Journal of Experimental Biology (2016) 219, 752-766 doi:10.1242/jeb.127829

speeds above $\sim 3c_{min}$, as Weber numbers increase and the relative dominance of surface tension decreases (Sun and Keller, 2001). However, this is well above the terminal velocities observed for interfacial flight.

Hence, interfacial flight is considerably more energetically expensive than airborne flight except either at very low or very high velocity. This simple calculation rules out energetic advantages for 2D flight in *G. nymphaeae*, primarily hinting towards its relevance either as a better search strategy in the 2D landscape on the water surface or as a viable low-speed alternative to self-supported airborne flight under conditions where flight muscles are less efficient.

Vertical oscillations play an important role in assisting take-off from the interface

We applied our dynamic model to understand how *G. nymphaeae* is consistently able to take off with ease using wing forces alone. Our observations of failed take-off attempts underline that surface tension is a powerful energy trap, which makes the net static force required to pull off the interface higher than that needed to stay aloft in air. This is also evident in many modern flying insects, such as flies and mosquitoes, which become trapped on a water surface when their limbs are wetted. However, though the static lift required to break off the interface is high, it is reduced for a dynamic flight sequence because of the significant inertial contribution from vertical oscillations. When the insect is in motion, the acceleration of the beetle produced by the oscillations is of the same order of magnitude as surface tension. Further, when directed opposite surface tension on rising above the water level, it cooperates with the wing lift to help the insect rise higher above the interface and break the meniscus. This reduces the net wing lift required to counter surface tension and body weight during take-off. As the oscillations responsible for assisting take-off arise from the interplay between wing force and the non-linear resultant of surface tension, it is expected that the relationship between take-off times and wingbeat parameters is complex and non-monotonic. Using a computational survey of parameter space, we explored the effect of wingbeat parameters on the take-off time for an insect in interfacial flight. We explored the effects of changing wingbeat frequency (Fig. 6C), the ratio of upstroke force to downstroke force (Fig. 6D) and the contact line radius at the legs (Fig. S4). This virtual parameter sweep allows us to study variations in individual flight parameters that are not possible to independently or physiologically manipulate in the real world, especially with all other factors kept constant. In Fig. 6C–E (2-leg flight) and Fig. S2A–C (4-leg flight), we see that isochronous contours for take-off time have very complex shapes, and that take-off is possible even below the static lift requirements. In the absence of effects like body angle variation and jumping, while the insect can take off from the interface instantly at high wing lifts, it remains trapped on the interface at lower lift magnitudes. In the intermediate regimes of lift where *G. nymphaeae* operates, it takes a certain amount of time to build up energy in meniscus oscillations and takes off from the interface with some delay. While take-off times range from a few milliseconds to a few seconds, we note that a significant proportion of trajectories have take-off times of the order of several wingbeats (tens of milliseconds). This is of the same order of time as the neural responses involved in active flight control in insects (Ristroph et al., 2010). For trajectories in these regimes, we infer that there is no active control of flight during take-off. It is therefore desirable that for passive stabilization, perturbations of the interfacial flight trajectory are not amplified. For the trajectory to remain stable during take-off, it is preferable for the system dynamics to be robust to disturbances over these time scales.

Surface tension drives chaotic oscillatory trajectories normal to the interface

We analysed the stability of interfacial flight dynamics to see whether small perturbations in the trajectory are damped out or amplified. The Lyapunov exponents are an indicator of the rate of change of a given trajectory in phase space along the dimensions represented by the chosen variables $\{t, y, \dot{y}\}$. (A rigorous analytical derivation of the Lyapunov exponents is given in the Appendix.) We obtain the signs $\{0,+,-\}$ for these exponents, implying divergence of perturbations along one dimension with a contraction in the other, which is characteristic of chaotic phase space trajectories (Dingwell, 2006). We constructed a bifurcation diagram to see how the periodicity of interfacial flight trajectories varies with the wing lift amplitude that forces the vertical oscillations (Fig. 7A). For an insect where both hindlegs and forelegs remain in contact with the interface throughout, there is initially a periodic regime at low values of the lift-to-weight ratio q. As q increases, several bifurcations lead to multi-periodic orbits, with aperiodic regimes beginning to appear between islands of periodic orbits as q approaches 1 – the minimum value of q needed to support the insect's body weight in air. These orbits include small period-three regions between q=1 and 1.1, which are a definite indicator of chaos in the system. There is a wide chaotic belt between $q \approx 1.1$ and 2.8, where most modern insects capable of airborne flight would be found. Trajectories begin to quickly take off from the interface as lift amplitudes exceed $q \approx 2.8$. Phase plots for two trajectories from the periodic and chaotic regimes show complex self-intersecting shapes when embedded in the $\{y, \dot{y}\}$ plane (Fig. 7B). It is interesting to note that the structure of the phase plot from the chaotic interfacial flight regime with q=1.48 (Fig. 7B, lower panel) strongly resembles that of another chaotic surface tension-based oscillator – the soap-film fluid trampoline (Gilet and Bush, 2009). Trajectories in the chaotic regime also display a sensitive dependence on initial conditions as shown in Fig. 7C, which is the hallmark of chaos in the system. To confirm that our mathematical prediction of chaos also applies to experimentally recorded trajectories, we constructed a delay plot (Fig. 7D) for the representative trajectory shown in Fig. 3A. The vertical displacement in this trajectory is uncorrelated across successive wingbeats, without any periodic or repeating structures. As the errors due to measurement are much smaller than the length scales for displacement, we conclude that the lack of correlation is truly a consequence of chaos and not an artefact of experimental noise. These results indicate that small fluctuations in an interfacial flight trajectory could lead to significant instabilities; hence, it is not possible to predict when the insect takes off from the interface in a chaotic regime.

DISCUSSION

This work provides the first biomechanical analysis of interfacial flight in any insect. The waterlily beetle *G. nymphaeae* is also capable of well-developed airborne flight, which indicates that interfacial flight is a derived adaptation to their aquatic ecological niche on the surface of a pond. We have demonstrated the dominant influence and unique role of interfacial forces like capillary–gravity wave drag and surface tension in interfacial flight. These non-linear forces add a hitherto unforeseen complexity to interfacial flight and differentiate it from conventional airborne flight.

Second, using high-speed videos of *G. nymphaeae* flight kinematics, we developed a quantitative model to capture the

Journal of Experimental Biology

Journal of Experimental Biology (2016) 219, 752-766 doi:10.1242/jeb.127829

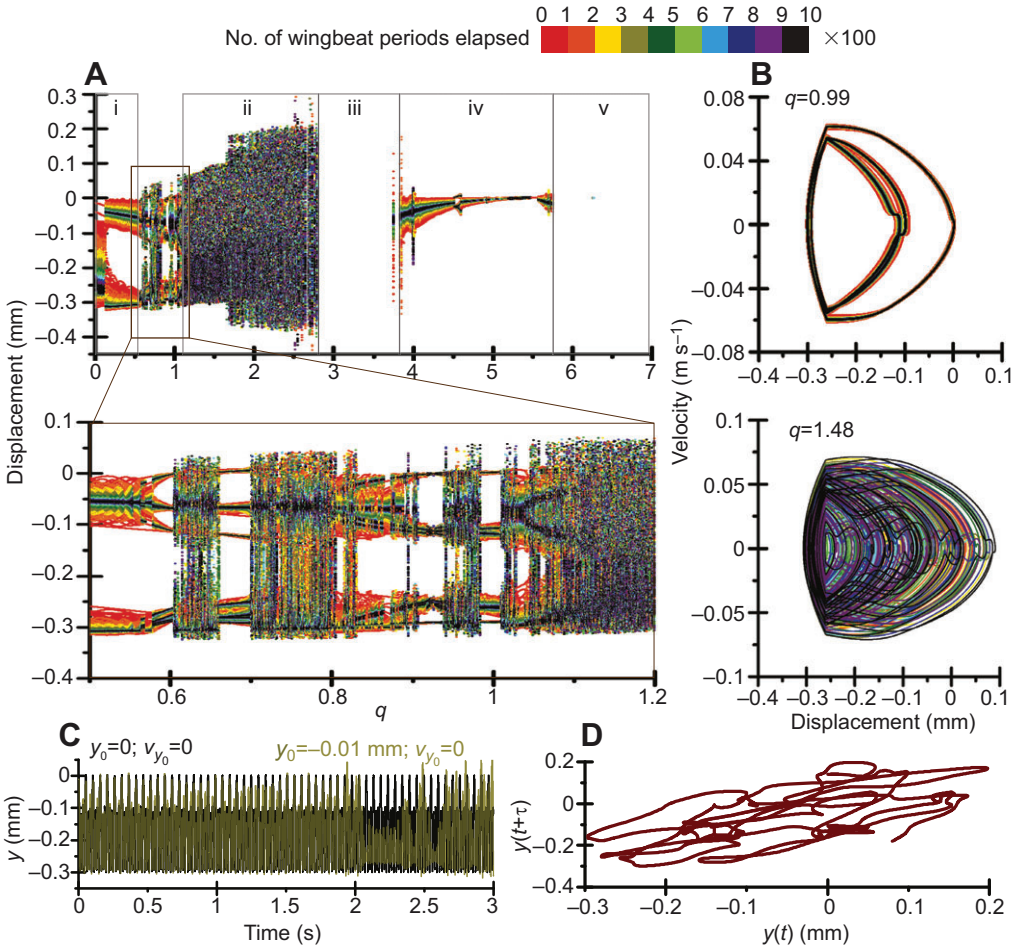

Fig. 7. Chaotic vertical oscillations on the interface. (A) Bifurcation diagram for trajectories at different lift-to-weight ratio q. A wide range of q shows five distinct trajectory regimes: (i) periodic and confined to interface, period equal to or half the wingbeat period; (ii) chaotic, confined to the interface; (iii) chaotic, takes off from the interface with some time delay; (iv) periodic and confined to interface, period equal to wingbeat period; (v) instantaneous take-off. The expanded section of the transition between regimes i and ii shows cascades and regions of chaos. (B) Phase plot at q=0.99 (top) shows a self-intersecting period-4 cycle. Phase plot at q=1.48 (bottom) shows a chaotic attractor also seen in other oscillators driven by surface tension (Gilet and Bush, 2009). (C) Divergence of two trajectories with closely spaced initial conditions in the chaotic regime (q=1.48), where one takes off and the other is trapped on the interface. Both trajectories are simulated with the parameters L=137 μN, f=116 Hz, r=0.15 and $\phi_0=\pi/2$, but for different initial conditions which do not lie on each other's $\{y, \dot{y}\}$ phase plot. (D) Delay plot of experimental trajectory data showing vertical displacement plotted against itself with a delay of τ=1 wingbeat≈8.67 ms. The lack of any repeated structure indicates that the vertical oscillations observed in the experimentally recorded trajectory do not have any correlation in time and are chaotic in nature.

fundamental physics underpinning interfacial flight. We speculate that an advantage of such fast locomotion is to avoid underwater predators like fish, which have been known to detect capillary waves on the surface of a pond generated by trapped insects that fall on the fluid surface (Schwarz et al., 2011). We have shown that manoeuvres in the transition between different flight modes – interfacial, airborne and backward – are controlled by postural changes. The body angle is the most probable tuning parameter used by the insect, being strongly correlated to the stroke plane angle and altering the ratio of lift and thrust produced by the wings. Our analysis also shows that at typical speeds, interfacial flight actually requires stronger wing thrust than airborne flight at the same speed, because of the high capillary gravity wave drag. We note, however, that *G. nymphaeae* clearly shows a preference for fast interfacial flight over airborne flight despite the higher energy expenditure. We suggest that the searching efficiency provided by 2D locomotion in foraging for floating food on a planar interface is sufficiently high to give this beetle a distinct advantage in staying on the interface. Another fascinating observation in many experiments is the lack of any active braking mechanism in 2D flight [Movie 3 (part A)]. We propose that the insect actually takes advantage of the high drag forces on the interface to passively manoeuvre, slow down or stop its motion during interfacial flight.

Third, using both successful (Movie 5) and failed (Movie 6) take-off attempts, we demonstrated that surface tension acts as an energy trap that necessitates enhanced lift production to take off from the interface. Take-off from a terrestrial surface into air is itself a complex and intriguing phenomenon in insect flight, needing mechanisms beyond wing flapping such as the ground effect and leg extension (Bimbard et al., 2013). The take-off of *G. nymphaeae* from a fluid interface into air gains further complexity, as there are additional surface tension forces tethering the insect to the interface. This argues against the hypothesis of a transition between interfacial and airborne flight simply by increasing wing force. However, it highlights the importance of additional take-off mechanisms as observed by Marden et al. (2000) and Bimbard et al. (2013), such as reducing the number of legs in contact with water or jumping off the surface. An important possible contribution to further enhancing the

wing lift produced by an insect in interfacial flight is the ground effect (Rayner and Thomas, 1991). The insect beats its wings barely a few millimetres above the water surface. The reflection of wingtip vortices from the water surface can increase the unsteady lift produced by the wings for the same biomechanical energy cost. *Galerucella nymphaeae* is an ideal model organism for future studies in this area.

Fourth, we have shown that interfacial fliers are assisted in breaking the meniscus and taking off from the interface by dynamic energy storage in vertical oscillations of the meniscus. The optimal conditions for minimizing either the time or the lift required for take-off are different, and have an intricate dependence on the wingbeat parameters. It is interesting to note that typical values of some of these parameters are far from optimal in *G. nymphaeae*. For example, the optimal frequency to take off from the interface using the minimum wing lift is 60 Hz for an insect in 4-leg interfacial flight (Fig. S2A), and about 30 Hz for an insect in 2-leg flight (Fig. 6C). However, the physiological value of wingbeat frequency is constant at about 116 Hz (Fig. S1A), which is far removed from these optimal frequencies. These oscillations of the meniscus can often lead to take-off at time scales that are comparable to the time required to mount an active neural response for flight control. This can pose challenges in controlling the take-off process, particularly when disturbances in the trajectory are amplified.

Finally, we have shown that interfacial flight is an example of chaos arising naturally in a biological system. The dependence of biological functions on chaotic rhythms has been demonstrated in systems as diverse as vortex interactions with flapping wings (Lentink et al., 2010), tidal bobbing in giant kelp (Denny et al., 1997), amputee runners adjusting their stability (Look et al., 2013), circadian rhythms in foraging ants (Nicolis et al., 2013), tumour necrosis factor (TNF)-driven inflammatory responses in cells (Jensen and Krishna, 2012), and turbulent flow-driven maturation in sea urchin larvae (Gaylord et al., 2013). In the context of interfacial flight dynamics, the emergence of chaotic trajectories hints at the challenge of developing robust flight control mechanisms on the interface, as higher lift magnitudes produce inherently unstable trajectories. Our work also opens up interesting possibilities for designing new kinds of robust control algorithms for bio-mimetic robots that operate on fluid interfaces.

Our discovery of complex interfacial flight behaviour in *G. nymphaeae* provides an excellent experimental platform to study the ground effect in insect flight, the kinematics and dynamics of the progression from interfacial to airborne flight, neural responses in a chaotic biological system, and new kinds of interfacial fluidic oscillators. The model of interfacial flight that we have presented provides a starting point for quantitatively understanding the basic underlying physics. This can be used as the basis for further refinement and also future studies on varied forms of interfacial flight and surface skimming in different organisms and robotic systems, with more detailed and organism-specific expressions for the individual forces involved. We hope that this work will open up new avenues for both experimental and analytical investigations into insect behaviour, biomechanics, robotics and interfacial fluid mechanics.

Appendix

Section 1 – analytical reduced-order model for interfacial flight

The forces acting on an insect in interfacial flight arise from four physical phenomena: (1) capillarity – capillary wave drag C_x (horizontal) and surface tension S_y (vertical); (2) aerodynamics – thrust T_x (horizontal), lift L_y (vertical) and air drag A_x (horizontal); (3) bulk hydrodynamics – water drag on immersed legs W_x, W_y (horizontal and vertical); (4) gravity – body weight G_y (vertical). Newton's second law of motion for this system is formulated in the horizontal (x) and vertical (y) axes as $m\ddot{x}=T_x-W_x-A_x-C_x$ and $m\ddot{y}=L_y-W_y-G_y-S_y$. The expressions for each of these forces are:

$$C_x \cong 4\times\rho_w c_{min}^2\kappa^{-1}\sqrt{\frac{\dot{x}}{c_{min}}-1}\times 2R_{claw}\times U(\dot{x}-c_{min}), \quad (A1)$$

$$S_y=\begin{pmatrix} 4\times 2\pi\sigma R_{claw}, & y<-H_{claw} \\ 4\times 2\pi\sigma R_{claw}\,\mathrm{sech}\left(\frac{y-H_{claw}}{R_{claw}}\right)\times\frac{-y}{|y|}, & -H_{claw}\le y\le H_{claw} \\ 0, & y>H_{claw}\end{pmatrix}, \quad (A2)$$

$$L_y=L\sin(2\pi ft+\phi_0)\times[U(\sin(2\pi ft+\phi_0))+r\{1-U(\sin(2\pi ft+\phi_0))\}], \quad (A3)$$

$$T_x=pL_y, \quad (A4)$$

$$A_x=\frac{1}{2}\rho_{air}C_{D,body}\pi ab\dot{x}^2, \quad (A5)$$

$$W_d=4\times\frac{1}{2}\rho_w C_{D,leg}\pi R_{claw}^2\dot{d}^2;\ d=x,y, \quad (A6)$$

$$G_y=-g. \quad (A7)$$

Below, we derive detailed expressions for each of these individual forces.

Capillary wave drag

The portion of the legs immersed just below the surface moves through the interface at speeds greater than capillary wave speed to give rise to this force. The legs have a characteristic radius of 57 µm, which is small compared with the capillary length κ^{-1}=2.709 mm, typical horizontal velocities ranging from 0.3 to 0.5 ms^{-1}, which is comparable to the capillary wave speed of 0.23 ms^{-1}, and Weber numbers of the order of 0.1, which is quite low. Hence, the dipolar approximation (Chepelianskii et al., 2010) at low Weber number can be used to compute the capillary wave drag force on each leg. Using the force normalized per unit transverse extent of the submerged object, we multiply this by the leg diameter to get the total force. We obtain the expression in Eqn A1:

$$C_x \cong 4\times\rho_w c_{min}^2\kappa^{-1}\sqrt{\frac{\dot{x}}{c_{min}}-1}\times 2R_{claw}\times U(\dot{x}-c_{min}). \quad (A8)$$

Surface tension

The surface tension on each leg is modelled assuming quasi-static deformation of non-interacting minimal surface menisci. These approximations are justified as the capillary relaxation time scale (≈50 µs) is much smaller than the inertial time scale (wingbeat period τ=8.67 ms), meaning that any flows within the meniscus or contact line hysteresis die out fast enough that they can be ignored

Journal of Experimental Biology

and meniscus deformations assumed to be instantaneous. Also, the meniscus maximum height (≈250 µm) is much smaller than the capillary length κ^{-1}=2.709 mm, which in turn is smaller than the physical separation between the legs corresponding to the beetle's body width and length of 4–6 mm, indicating that the menisci are minimal surfaces placed far enough apart that their finite physical size is too small for them to interact. The four legs immersed in water are modelled as non-interacting infinite fibres, each of which forms a minimal surface meniscus with the contact line pinned at the line barrier between the superhydrophobic tarsus and the hydrophilic claw (de Gennes et al., 2004). The meniscus is described as the minimal curve:

$$x = R_{\text{claw}} \cosh\left(\frac{y - H_{\text{claw}}}{R_{\text{claw}}}\right). \tag{A9}$$

This minimal curve assumption was experimentally verified by numerically fitting the meniscus produced by dipping the claw of a dead beetle in water and pulling it up to create a meniscus of known vertical height (Fig. 2J). The weight of water in the meniscus is supported by gravity, and hence the maximum height where the meniscus becomes too heavy and breaks is:

$$H_{\text{claw}} = R_{\text{claw}} \ln\left(\frac{2\kappa^{-1}}{R_{\text{claw}}}\right) \tag{A10}$$

when its horizontal extent reaches the capillary length.

There are three different cases possible for surface tension. First, when the leg is immersed deeper than the tarsal-claw joint, we assume contact angle is always 0 deg and the contact line slips along the tarsus. Second, when the leg rises above the maximum vertical extent of the meniscus, the meniscus breaks, releasing the leg from contact with water and there is no more surface tension, unless the leg descends sufficiently to become re-immersed in water. Third, in the normally observed case, the leg has an intermediate displacement with contact angle being a function of displacement. Here, the contact angle θ at the fibre is calculated from the slope of the meniscus as:

$$\cos\ \theta = \operatorname{sech}\left(\frac{y - H_{\text{claw}}}{R_{\text{claw}}}\right). \tag{A11}$$

Taking these three regimes into account, the resultant force from surface tension (de Gennes et al., 2004) is expressed in Eqn A2 as:

$$S_y = \begin{pmatrix} 4 \times 2\pi\sigma R_{\text{claw}}, & y < -H_{\text{claw}} \\ 4 \times 2\pi\sigma R_{\text{claw}} \operatorname{sech}\left(\frac{y - H_{\text{claw}}}{R_{\text{claw}}}\right) \times \frac{-y}{|y|}, & -H_{\text{claw}} \le y \le H_{\text{claw}} \\ 0, & y > H_{\text{claw}} \end{pmatrix}. \tag{A12}$$

To represent the transition from 2D flight to airborne flight, we define a take-off time t_{to}, which is the last instant during a trajectory where the claw is in contact with water.

Thrust and lift

For the wing force, the contribution of ground effect (Rayner and Thomas, 1991) due to interaction with the deformable water surface is unknown, and the exact variation of force with stroke position is also unknown for this system. Hence, we loosely approximate wing force as a sinusoid (Dudley, 2000) with a fixed wingbeat frequency f=116 Hz, as the kinematics of the wing tip follows a sinusoidal trajectory. We parameterize this expression with variables for amplitude of lift force L, ratio of thrust to lift p, wing stroke angle at initiation of motion ϕ_0 and ratio of forces produced in upstroke and downstroke r – as all of these can vary for each trajectory at the will of the insect, and cannot be easily measured without perturbing the insect. The total wing force is resolved into the two components of vertical lift and horizontal thrust in Eqns A3 and A4:

$$L_y = L \sin(2\pi f t + \phi_0) \times [U(\sin(2\pi f t + \phi_0)) + r\{1 - U(\sin(2\pi f t + \phi_0))\}] \tag{A13}$$

$$T_x = pL_y. \tag{A14}$$

Here, U is the Heaviside step function.

Air drag

To compute the aerodynamic drag, the beetle's body is approximated as an ellipsoidal bluff body in cross-flow, with the flow incident on the ventral surface of the insect's body. Air drag on the body is given in Eqn A5 by:

$$A_x = \frac{1}{2}\rho_{\text{air}} C_{\text{D,body}} \pi a b \dot{x}^2, \tag{A15}$$

where a=6 mm and b=4 mm are the major and minor axes of the ellipse formed by the body cross-section and $C_{\text{D,body}}$≈1.5 is a typical body drag coefficient for insects of similar size and profile (Nachtigall, 1991).

Water drag

For drag from water, we roughly approximate the pair of curved claws as a sphere, whose radius is assumed to be equal to the radius of the leg at the claw joint, R_{claw}=57 µm. Drag forces from water are expressed for spheres in cross-flow in Eqn A6 as:

$$W_d = 4 \times \frac{1}{2}\rho_{\text{w}} C_{\text{D,leg}} \pi R_{\text{claw}}^2 \dot{d}^2; \quad d = x, y, \tag{A16}$$

where $C_{\text{D,leg}}$≈3 is the drag coefficient for a sphere in cross-flow at the appropriate Reynolds number range 10<Re<100, and $\dot{d} = \dot{x}, \dot{y}$, respectively, for horizontal and vertical drag forces.

Gravity

The body weight is given by mg, where m≈2.2 mg is the average weight of the insect calculated by averaging weights for about 30 dead insects; g=9.81 ms^{-2} is the acceleration due to gravity.

Validation

Simulations of the dynamics were performed in MATLAB R2012b using a built-in ODE solver (ode113), with relative tolerances of 10^{-9} and a constant integration time step of 10^{-8} s. The elimination of numerical noise was verified by computing take-off times for a variety of different thrust-to-lift ratios p keeping other parameters constant, and checking that take-off time is repeatedly constant for a given lift L at the required precision, as expected from decoupling of horizontal and vertical dynamics.

In our experiments on live *G. nymphaeae*, there are natural variations in initial displacements and velocities $\{x_0, \dot{x}_0, y_0, \dot{y}_0\}$, wingbeat frequency f, magnitude of wing lift L, thrust-to-lift ratio p, initial wing stroke angle ϕ_0, and ratio of forces generated in upstroke and downstroke r. These nine parameters can even vary within a single trajectory, typically in the initial stages of flight when the insect has yet to settle into a consistent rhythm. Moreover, many of these, such as L, p, ϕ_0 and r, are not directly measurable quantities. As this non-linear system is expected to be sensitive to even small variations in these parameters, it is not possible to sweep across all of them to exactly fit each experimentally obtained trajectory. Hence,

we validated our model by ensuring that simulated trajectories capture four basic kinematic features common to all experimental trajectories: (1) horizontal displacement has sigmoidal variations in each wingbeat superimposed on a quadratically increasing profile, covering between 15 and 25 mm in about 100 ms; (2) horizontal velocity varies sinusoidally in each wingbeat, with the mean rising linearly to 0.25 to 0.5 ms^{-1} before levelling off; (3) vertical displacement should show oscillations of amplitude 0.2 and 0.5 mm and frequency approximately equal to wingbeat; (4) the peak displacement in each oscillation should vary in height.

Our model was able to reproduce simulated trajectories with these characteristics for physiologically feasible ranges of the parameters, as shown in Fig. S3. Thus, we validate that our model is a good approximation that captures the most basic and essential physics involved in interfacial flight.

Section 2 – drag force calculations

Consider a typical flight speed of the insect around 0.3 m s^{-1}. We refer to equations for drag forces derived in section 1. We assume that the insect has a similar profile when flying in air or on the interface, with a comparable cross-sectional body area. For an insect flying in air, air drag estimated using Eqn A5 is around $A_x=\frac{1}{2}\rho_{air}C_{D,body}\pi ab\dot{x}^2\approx 6$ N, using values of a=6 mm, b=4 mm and $C_{D,body}\approx 1.5$. For an insect flying on the interface, the same air drag is experienced. In addition, there is capillary–gravity wave drag, which is estimated from Eqn A1 as $C_x\cong 4\times\rho_w c_{min}^2\kappa^{-1}\sqrt{\frac{\dot{x}}{c_{min}}-1}\times 2R_{claw}\times U(\dot{x}-c_{min})\approx 36$ μN. Hence, the total drag in interfacial flight is 42 μN, which is about 7 times the drag in airborne flight. Air drag increases as the square of the velocity, which is a faster rise than capillary drag, which increases as the square root of the velocity. However, the two become approximately equal only at $\dot{x}\approx 1.52$ m s^{-1}, which is an extremely high speed for interfacial motion!

Section 3 – lift coefficient (C_L) estimation

We assume that the force generated by the wings during stalled vertical take-off is entirely directed into vertical lift, and that the contact angle on the two wetted legs is 180 deg. As the insect is in static equilibrium, we estimate the lift using Eqn 3 to be $L_{max}=2\times(2\pi\sigma R_{claw})+mg=73.2$ μN. Parameters of the wing stroke are measured from Movie 2 (part C), having a resolution of 115 μm. The wing chord is measured to be C=5.6 mm. We measured the typical stroke angle as ϕ=120 deg using Movie 2 (part C), which has a rear view. For a wingbeat frequency of ν=3000/26 Hz, this corresponds to a wing angular velocity of $\omega=2\phi\nu$=483 rad s^{-1}. Wingtip velocity is thus $V_w=C_\omega$=2.7 m s^{-1}. Drawing a free-hand tool outline around the face-on view of the wing in mid-stroke gives a wing area A_w=11 mm^2, measured using ImageJ. For verification, measuring wing chord and the broadest part of the wing in the vertical direction to be 5.6 and 2.8 mm, respectively, and assuming an elliptical wing gives an area of $[(\pi/4)C_\omega\approx 12\ mm^2]$, which is close to the measured value. Hence, we can compute an approximate lift coefficient for the wing $C_L\cong L_{max}/0.5\rho_{air}A_wV_w^2=1.55$.

Section 4 – characteristics of Lyapunov exponents

Consider the dynamic equation for vertical motion for the vector $\vec{Y}=\{t,y,\dot{y}\}$ in phase space, for the case where the beetle is continuously attached to the interface, i.e. $y\le H_{claw},\forall t\ge 0$. The second order inhomogeneous ordinary differential equation can be written as a set of first order ordinary differential equations as:

$$\frac{d\vec{Y}}{dt}=\begin{bmatrix}1\\ \dot{y}\\ \ddot{y}\end{bmatrix}=\begin{bmatrix}1\\ \dot{y}\\ \left\{\frac{L}{m}\cos(2\pi ft+\phi_0)[U(\sin(2\pi ft+\phi_0))+r(1-U(\sin(2\pi ft+\phi_0)))]\right\}\\ -\left\{\frac{8\pi\sigma R_{claw}}{m}\,\mathrm{sech}\left(\frac{y-H_{claw}}{R_{claw}}\right)\mathrm{sgn}(y)\right\}\\ -\left\{\frac{2\rho_w C_{D,leg}\pi R_{claw}^2}{m}\,\dot{y}\,\mathrm{sgn}(\dot{y})\right\}\end{bmatrix}. \quad (A17)$$

For any small perturbation $\vec{\varepsilon}$, $\frac{d\vec{\varepsilon}}{dt}=\mathbb{J}\cdot\vec{\varepsilon}$, where $\mathbb{J}$ is the Jacobian matrix for the system, given by:

$$\mathbb{J}=\begin{bmatrix}0&0&0\\0&0&1\\ \alpha&\beta&\gamma\end{bmatrix}, \quad (A18)$$

where:

$$\alpha=\left\{\frac{L}{m}\cos(2\pi ft+\phi_0)[U(\sin(2\pi ft+\phi_0))+r(1-U(\sin(2\pi ft+\phi_0)))]\right\}$$

$$\beta=\left\{\frac{8\pi\sigma R_{claw}}{m}\mathrm{sech}\left(\frac{y-H_{claw}}{R_{claw}}\right)\tanh\left(\frac{y-H_{claw}}{R_{claw}}\right)\mathrm{sgn}(y)\right\}$$

and

$$\gamma=\left\{\frac{-4\rho_w C_{D,leg}\pi R_{claw}^2}{m}|\dot{y}|\right\}.$$

The eigenvalues of $\mathbb{J}$ are $\lambda_1=0,\lambda_{2,3}=-\mathbb{A}\pm\sqrt{\mathbb{A}^2+\mathbb{B}}$, where:

$$\mathbb{A}=\frac{2\pi\rho_w C_{D,leg}R_{claw}^2}{m}|\dot{y}|, \quad (A19)$$

$$\mathbb{B}=\frac{8\pi\sigma R_{claw}}{m}\mathrm{sech}\left(\frac{y-H_{claw}}{R_{claw}}\right)\tanh\left(\frac{y-H_{claw}}{R_{claw}}\right)\mathrm{sgn}(y). \quad (A20)$$

$\lambda_{2,3}\epsilon\mathbb{R}$ for values of $\mathbb{A}^2+\mathbb{B}\ge 0$ and $(\lambda_2\times\lambda_3)<0$ for $\Rightarrow\lambda_{2,3}\epsilon\mathbb{R}\ \&\ (\lambda_2\times\lambda_3)\langle 0\ \forall\ \mathbb{B}\rangle 0$,

$$\Rightarrow\lambda_{2,3}\epsilon\mathbb{R}\ \&\ (\lambda_2\times\lambda_3)\langle 0\ \forall\ \mathbb{B}\rangle 0, \quad (A21)$$

$$\mathrm{sech}\left(\frac{y-H_{claw}}{R_{claw}}\right)\tanh\left(\frac{y-H_{claw}}{R_{claw}}\right)\mathrm{sgn}(y)>0. \quad (A22)$$

In the domain $y \leq H_{\text{claw}}$, $\operatorname{sech}\left(\frac{y - H_{\text{claw}}}{R_{\text{claw}}}\right) > 0$ and $\tanh\left(\frac{y - H_{\text{claw}}}{R_{\text{claw}}}\right) < 0$ always, $\Rightarrow \operatorname{sgn}(y) < 0$.

$\therefore$ Eigenvalues of $\mathbb{J}$ are real and of opposite signs for $-H_{\text{claw}} \leq y < 0$.

The transformation matrix for this system is $\Phi(t) = \exp \int_0^t \mathbb{J} \mathrm{d}t$.

The Lyapunov exponents of the system are hence equal to the eigenvalues λ_i of $\mathbb{J}$:

$$\det |\Phi(t)| = \det \left| \exp \int_0^t \mathbb{J} \mathrm{d}t \right| = \exp \left(\sum_{i=1}^{3} \lambda_i t \right), \tag{A23}$$

$\Rightarrow l \lim_{t \to \infty} \frac{1}{t} \ln(\det |\Phi(t)|) = -2\mathbb{A}$, which is finite and exists $\forall t$. $\lim_{t \to \infty} \frac{1}{t} \ln(\det |\Phi(t)|) = \sum_{i=1}^{3} \lambda_i$ for the $\mathbb{R}^3$ basis:

$$\begin{bmatrix} 1 \\ 0 \\ 0 \end{bmatrix}, \quad \begin{bmatrix} 0 \\ 1 \\ 0 \end{bmatrix}, \quad \begin{bmatrix} 0 \\ 0 \\ 1 \end{bmatrix}.$$

Hence, the vertical dynamics has a transformation matrix $\phi(t)$ which is regular, implying that the Lyapunov exponents λ_i, i=1,2,3 exist and are finite for all perturbations of trajectories and are independent of the initial conditions.

In the domain $-H_{\text{claw}} \leq y \leq H_{\text{claw}}$, $\sum_{i=1}^{3} \lambda_i = -2\mathbb{A} < 0$ always, hence the system is always dissipative, as expected of motion under drag forces. Additionally, when $-H_{\text{claw}} \leq y < 0$, the exponents λ_2, λ_3 are real and of opposite signs. Hence, those regimes of a trajectory where $-H_{\text{claw}} \leq y < 0$ evolve along chaotic attractors. Therefore, every trajectory that lies at least partially in a region of phase space where these two conditions hold true displays chaotic behaviour. The downward pull of gravity on the beetle results in the equilibrium vertical displacement being below the mean water level at infinity ($y_{\text{eq}} < 0$). Therefore, at low values of lift force L, the resulting oscillatory trajectories confined to the interface typically have $y < 0$ for significant continuous portions of the trajectory, resulting in chaotic motion.

Acknowledgements

We acknowledge all members of the Prakash Lab at Stanford University for meaningful advice and insights. We specifically acknowledge high school student Aditya Gande, who wrote the code for automated tracking of insect flight. We also acknowledge Harvard Forest for providing a place to collect insects, and Harvard Society of Fellows for providing a place to freely contemplate some of the ideas presented here. Finally, we acknowledge our reviewers for their insightful comments on our manuscript.

Competing interests

The authors declare no competing or financial interests.

Author contributions

M.P. discovered interfacial flight in beetles in the field. T.C.B., D.H.K., H.M. and M.P. collected further field and laboratory data. H.M. and M.P. analysed the data, developed the dynamical system model and wrote the manuscript.

Funding

H.M. acknowledges support from the Howard Hughes Medical Institute International Student Research Fellowship. M.P. acknowledges funding from the National Science Foundation (NSF) Career Award and the Pew Foundation Fellowship. Deposited in PMC for release after 6 months.

Supplementary information

Supplementary information available online at http://jeb.biologists.org/lookup/suppl/doi:10.1242/jeb.127829/-/DC1

References

Barthlott, W., Schimmel, T., Wiersch, S., Koch, K., Brede, M., Barczewski, M., Walheim, S., Weis, A., Kaltenmaier, A., Leder, A. et al. (2010). The Salvinia paradox: superhydrophobic surfaces with hydrophilic pins for air retention under water. *Adv. Mater.* **22**, 2325-2328.

Bimbard, G., Kolomenskiy, D., Bouteleux, O., Casas, J. and Godoy-Diana, R. (2013). Force balance in the take-off of a pierid butterfly: relative importance and timing of leg impulsion and aerodynamic forces. *J. Exp. Biol.* **216**, 3551-3563.

Bush, J. W. M. and Hu, D. L. (2006). Walking on water: biolocomotion at the interface. *Annu. Rev. Fluid Mech.* **38**, 339-369.

Bush, J. W. M., Hu, D. L. and Prakash, M. (2008). The integument of water-walking arthropods: form and function. *Adv. Insect Physiol.* **34**, 117-192.

Chepelianskii, A. D., Schindler, M., Chevy, F. and Raphaël, E. (2010). Self-consistent theory of capillary-gravity-wave generation by small moving objects. *Phys. Rev. E* **81**, 016306.

de Gennes, P.-G., Brochard-Wyart, F. and Quéré, D. (2004). *Capillary and Wetting Phenomena*. New York: Springer.

Denny, M. W., Gaylord, B. P. and Cowen, E. A. (1997). Flow and flexibility. II. The roles of size and shape in determining wave forces on the bull kelp *Nereocystis luetkeana*. *J. Exp. Biol.* **200**, 3165-3183.

Dickinson, M. H., Lehmann, F.-O. and Sane, S. P. (1999). Wing rotation and the aerodynamic basis of insect flight. *Science* **284**, 1954-1960.

Dingwell, J. B. (2006). Lyapunov exponents. *Wiley Encyclopedia of Biomedical Engineering*.

Dudley, R. (2000). *The Biomechanics of Insect Flight. Form, Function, Evolution*. Princeton, NJ: Princeton University Press.

Dudley, R. and Yanoviak, S. P. (2011). Animal Aloft: the origins of aerial behavior and flight. *Int. Comp. Biol.* **51**, 926-936.

Dudley, R., Byrnes, G., Yanoviak, S. P., Borrell, B., Brown, R. M. and McGuire, J. A. (2007). Gliding and the functional origins of flight: biomechanical novelty or necessity? *Annu. Rev. Ecol. Syst.* **38**, 179-201.

Ellington, C. P. (1995). Unsteady aerodynamics of insect flight. *Symp. Soc. Exp. Biol.* **49**, 109-129.

Gaylord, B., Hodin, J. and Ferner, M. C. (2013). Turbulent shear spurs settlement in larval sea urchins. *Proc. Natl. Acad. Sci. USA* **110**, 6901-6906.

Gilet, T. and Bush, J. W. M. (2009). The fluid trampoline: droplets bouncing on a soap film. *J. Fluid Mech.* **625**, 167-203.

Jensen, M. H. and Krishna, S. (2012). Inducing phase-locking and chaos in cellular oscillators by modulating the driving stimuli. *FEBS Lett.* **586**, 1664-1668.

Lehmann, F.-O. (2008). When wings touch wakes: understanding locomotor force control by wake wing interference in insect wings. *J. Exp. Biol.* **211**, 224-233.

Lentink, D., Van Heijst, G. F., Muijres, F. T. and Van Leeuwen, J. L. (2010). Vortex interactions with flapping wings and fins can be unpredictable. *Biol. Lett.* **6**, 394-397.

Look, N., Arellano, C. J., Grabowski, A. M., McDermott, W. J., Kram, R. and Bradley, E. (2013). Dynamic stability of running: the effects of speed and leg amputations on the maximal Lyapunov exponent. *Chaos* **23**, 043131.

Marden, J. H. (1987). Maximum lift production during take-off in flying animals. *J. Exp. Biol.* **130**, 235-258.

Marden, J. H. (2003). The surface-skimming hypothesis for the evolution of insect flight. *Acta Zool.* **46**, 73-84.

Marden, J. H. and Kramer, M. G. (1994). Surface-skimming stoneflies: a possible intermediate stage in insect flight evolution. *Science* **266**, 427-430.

Marden, J. H., O'Donnell, B. C., Thomas, M. A. and Bye, J. Y. (2000). Surface-skimming stoneflies and mayflies: the taxonomic and mechanical diversity of two-dimensional aerodynamic locomotion. *Physiol. Biochem. Zool.* **73**, 751-764.

May, R. M. (1988). How many species are there on Earth? *Science* **241**, 1441-1449.

Nachtigall, W. (1991). Aerodynamic coefficients for hymenopteran bodies. *Naturwissenschaften* **78**, 567-569.

Nicolis, S. C., Fernandez, J., Perez-Penichet, C., Noda, C., Tejera, F., Ramos, O., Sumpter, D. J. T. and Altshuler, E. (2013). Foraging at the edge of chaos: internal clock versus external forcing. *Phys. Rev. Lett.* **110**, 268104.

Prakash, M. and Bush, J. W. M. (2011). Interfacial propulsion by directional adhesion. *Intl. J. Non-Lin. Mech.* **46**, 607-615.

Raphael, E. and de Gennes, P.-G. (1996). Capillary gravity waves caused by a moving disturbance: wave resistance. *Phys. Rev. E* **53**, 3448-3455.

Rayner, J. M. V. and Thomas, A. L. R. (1991). On the vortex wake of an animal flying in a confined volume. *Philos. Trans. Biol. Sci.* **334**, 107-117.

Ristroph, L., Bergou, A. J., Ristroph, G., Coumes, K., Berman, G. J., Guckenheimer, J., Wang, J. Z. and Cohen, I. (2010). Discovering the flight autostabilizer of fruit flies by inducing aerial stumbles. *Proc. Natl. Acad. Sci. USA* **107**, 4820-4824.

Sane, S. P. (2003). The aerodynamics of insect flight. *J. Exp. Biol.* **206**, 4191-4208.

Schwarz, J. S., Reichenbach, T. and Hudspeth, A. J. (2011). A hydrodynamic sensory antenna used by killifish for nocturnal hunting. *J. Exp. Biol.* **214**, 1857-1866.

Simon, S., Strauss, S., Von Haeseler, A. and Hadrys, H. (2009). A phylogenomic approach to resolve the basal pterygote divergence. *Mol. Biol. Evol.* **26**, 2719-2730.
Sun, S.-M. and Keller, J. B. (2001). Capillary-gravity wave drag. *Phys. Fluids* **13**, 2146-2151.
Sun, M. and Tang, J. (2002). Lift and power requirements of hovering flight in *Drosophila virilis*. *J. Exp. Biol.* **205**, 2413-2427.
Suter, R. B., Rosenberg, R., Loeb, S., Wildman, H. and Long, J. H., Jr (1997). Locomotion on the water surface: propulsive mechanisms of the fisher spider *Dolomedes triton*. *J. Exp. Biol.* **200**, 2523-2538.
Voise, J. and Casas, J. (2010). The management of fluid and wave resistances by whirligig beetles. *J. R. Soc. Interface* **7**, 343-352.
Yanoviak, S. P., Dudley, R. and Kaspari, M. (2005). Directed aerial descent in canopy ants. *Nature* **433**, 624-626.

Journal of Experimental Biology

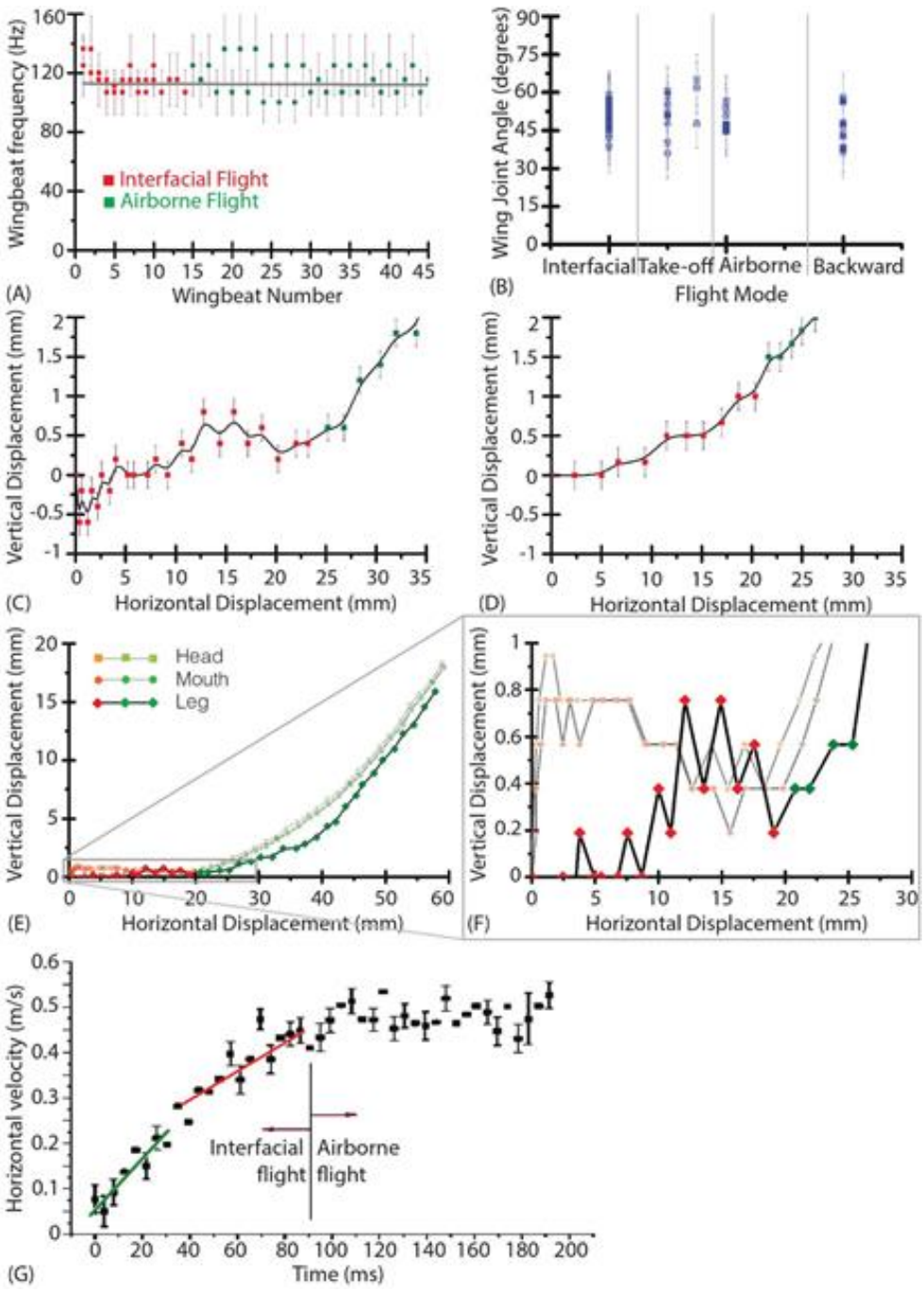

Fig. S1. Kinematics of additional interfacial flight trajectories

A, Plot of wingbeat period across wingbeats. Error bars are derived assuming deviations of one frame duration. **B**, Plot of wing joint angle across flight modes, calculated as sum of stroke plane angle and body angle, showing low variation across different flight modes. Error bars are estimated from pixel resolution error in extreme wing and body points used to calculate angles. **C,D**, Trajectories for additional flight sequences showing both interfacial flight with oscillations and airborne flight. Errors bars correspond to pixel resolution. **E**, Plot of trajectory for flight sequence as extracted at head, mouthparts and hind leg. **F**, Close-up showing pronounced discrepancies between trajectories measured at head and hind leg for interfacial flight. **G**, Average horizontal velocity for a flight trajectory, showing different accelerations (slopes) below and above the threshold velocity $c_{min} = 0.23\ ms^{-1}$ for the onset of capillary gravity wave drag.

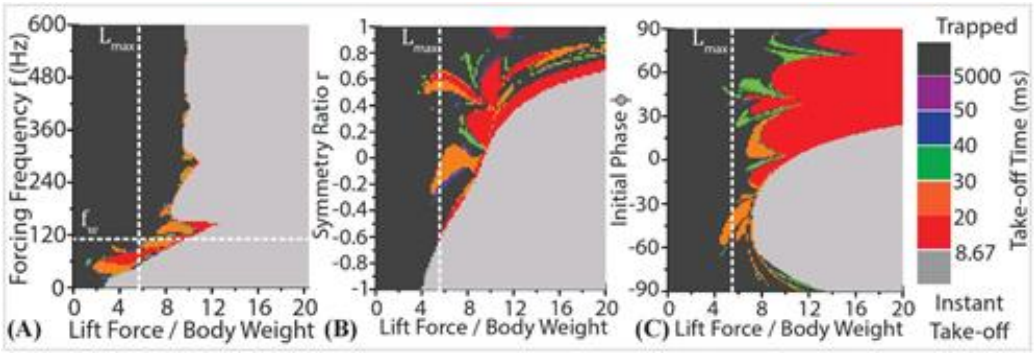

Fig. S2. Variation of take-off time with wing forcing parameters for 4-leg flight

A-C, Phase plots for variation in take-off time for different values of lift force per unit body weight. The single other parameter varied in each plot is wingbeat frequency in (**A**), symmetry ratio (r) between wing force produced in upstroke and downstroke in (**B**), and wing stroke angle at initiation of motion in (**C**). White dotted lines show maximum estimated lift $L_\sigma + 1 = 2 * (2\pi R_{claw}\sigma) + mg$ and wingbeat frequency f_w.

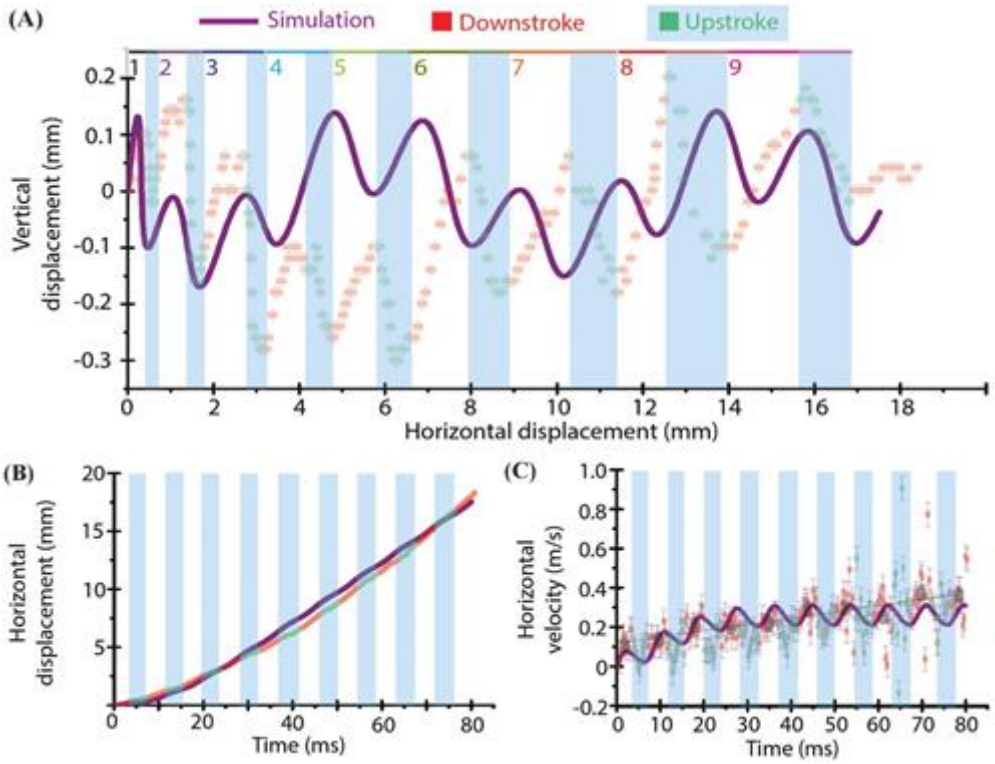

Fig. S3. Validation of dynamic model by matching major kinematics trends
Simulated trends are shown in violet and superimposed on experimental data shown in Figure 3. **A**, Trends are matched in horizontal displacement covered in 9 wingbeats, and the presence of vertical oscillations of varying peak level and amplitude of the same extent as meniscus deformation. **B**, Horizontal displacement in simulated trajectory closely matches experimentally obtained data. **C**, Horizontal velocity in simulated trajectory has similar magnitude and trends as experimentally obtained data.

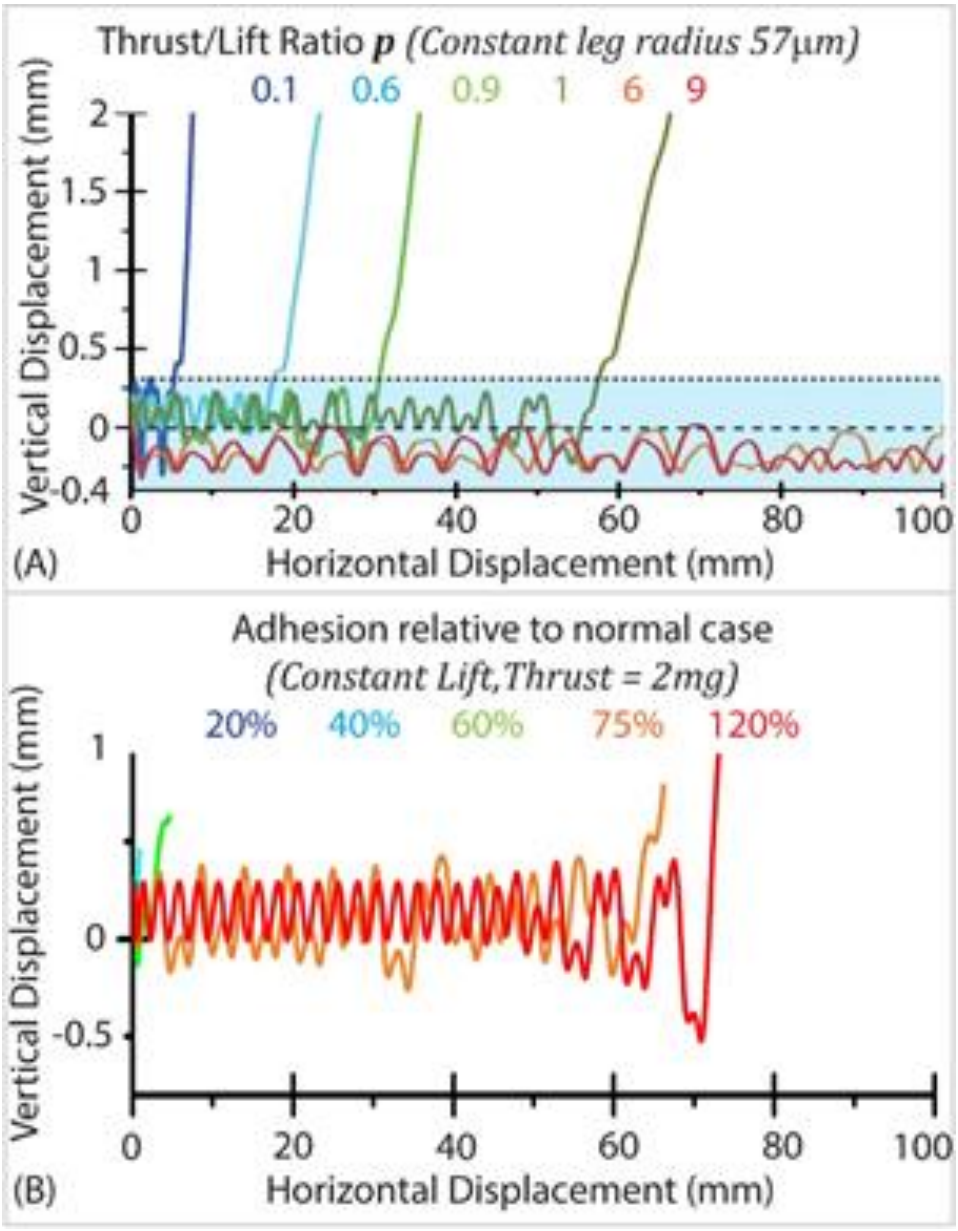

Fig. S4. Effect of varying thrust-to-lift ratio and leg radius (adhesion due to surface tension)
A, Computational modelling of trajectory variations due to **A**, different thrust-to-lift ratio at constant surface tension adhesion (leg radius) and **B**, varying surface tension adhesion (leg radius) at constant lift and thrust. It can be seen that when surface tension is reduced, the insect needs far less lift to take off from the surface. However, it also does not cover much horizontal distance as it simply doesn't stay on the surface long enough. It can remain on the surface by reducing the total wing force, but this would not enable it to develop high velocities along the interface. A strategy which would allow the insect to skim quickly for longer distance along the surfaces and then take off is by channeling the entire wing force into thrust with very little lift, which gives rise to horizontal motion. Changing the wing angle to increase lift gives rise to take-off, as indicated by Fig. 5A where flight mode is strongly correlated with stroke plane angle. It is important to note further that such a mechanism is independent of the actual values of lift and adhesion from surface tension, depending simply on the relative magnitudes of the two.

Movie 1: Close-up side views of interfacial flight
Part A: Side view close-up of interfacial flight in *Galerucella nymphaeae.* Side view close-up video of interfacial flight, used for trajectory extraction. The hind leg femur-tibia joint is visible as a dark spot, and was tracked across images. Note the initial lifting of the middle legs prior to flight. Recorded at 3000 fps, playback at 15 fps. Beetle body length is 6 mm. Part B: Side view of interfacial flight Side view close-up of initial posture adjustment and initiation of interfacial flight, showing postural changes and highlighting the role of the immersed claw in contact line pinning. Recorded at 3000 fps, playback at 30 fps. Beetle body length is 6 mm.

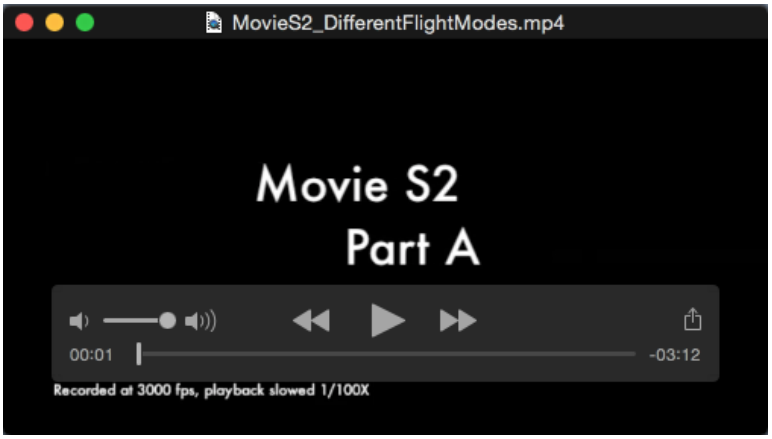

Movie 2: Various modes of flight in *G. nymphaeae.*
Part A: Seamless interfacial flight and take-off into air. Smooth variation between interfacial and airborne flight in a single flight sequence. Recorded at 3000 fps, playback at 30 fps. Beetle body length is 6 mm. Part B: Front view of take-off into air. Front view of *G.nymphaeae* taking off from the water surface. Recorded at 3000 fps, playback at 20 fps. Beetle body length is 6 mm. Part C: Rear view close-up of take-off into air. Rear view close-up of initial posture adjustment and initiation of interfacial flight. Recorded at 3000 fps, playback at 30 fps. Beetle body width is 4 mm. Part D: Backward flight. Backward movement of beetle in air on taking off from a pedestal. Recorded at 1000 fps, playback at 20 fps. Beetle body length is 6 mm.

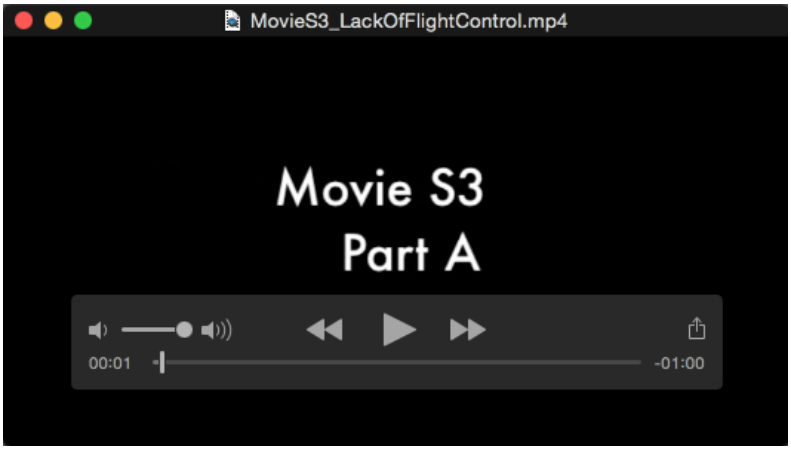

Movie 3: Loss of flight control on the interface. Part A: Lack of braking mechanism in interfacial flight. Interfacial flight sequence in G.nymphaeae on the surface of water in a Petri dish, where the insect does not stop but falls off the edge. Recorded at 3000 fps, playback at 30 fps. Beetle body length is 6 mm. Part B: Flight tumbling. Tumbling of beetle during 2D flight on a dish and subsequent recovery of upright posture. Recorded at 30 fps, playback at 30 fps (real time). Beetle body length is 6 mm.

Movie 4: Capillary wave formation. Formation of capillary waves on the surface of water during interfacial flight, visible as distortions of the edges of the water dish and optical posts supporting the experimental setup. Recorded at 3000 fps, playback at 30 fps. Beetle body length is 6 mm.

Movie 5: Breaking of meniscus during take-off. Formation of meniscus at the hind legs, which is lifted up to maximum height and subsequently breaks contact during take-off, setting up small ripples on the interface. Recorded at 3000 fps, playback at 30 fps. Beetle body length is 6 mm.

Movie 6: Failed take-off flight. Failed take-off attempt where take-off failed due to wetting of the beetle's hind legs. Initial detachment of middle legs from the surface and postural tilt of the beetle's body axis from horizontal to vertical are clearly seen, although pixel resolution is insufficient to accurately measure meniscus deformations. Recorded at 3000 fps, playback at 30 fps. Beetle body length is 6 mm.